https://doi.org/10.5194/egusphere-2023-978
Preprint. Discussion started: 22 June 2023

Surface Rupture Kinematics of the 2020 *Mw*6.6 Masbate (Philippines) Earthquake determined from Optical and Radar Data

Khelly Shan Sta. Rita[1], Sotiris Valkaniotis[2], and Alfredo Mahar Francisco Lagmay[1,3]

[1]National Institute of Geological Sciences, University of the Philippines, Diliman, Quezon City, Philippines 1101
[2]Department of Civil Engineering, Democritus University of Thrace, Xanthi, Greece 67100
[3]UP Resilience Institute, University of the Philippines, Diliman, Quezon City, Philippines 1101

Correspondence: Khelly Shan Sta. Rita (kcstarita@up.edu.ph)

Abstract. Optical correlation, interferometry, and field investigation of laterally offset features were undertaken to analyze the kinematics of the 2020 M_w6.6 Masbate earthquake. Coseismic displacement fields from optical correlation show a maximum displacement of 0.61 m corresponding to M_w6.64 geodetic moment magnitude and a lone asperity in Cataingan. Post-seismic deformation from interferometry highlights a maximum 0.14 m sinistral displacement equivalent to a M_w6.15 post-seismic moment magnitude, with coincident afterslip and coseismic slip distributions. The measured slip decreased towards the north, suggesting the presence of a slip barrier where stress can accumulate. Slip measurements and rupture length estimates characterize the Masbate segment as capable of producing unusually long ruptures with significant offsets despite the presence of creep. Post-seismic interferograms resolved the rupture far better than optical correlation, which was degraded due to high amplitude noise from sensor and environmental sources. Nevertheless, the resultant surface rupture morphology, as observed in optical correlation outputs and interferograms, demonstrated the presence of two transtensional basins in the north and south of the province, interlinked by a stepover of the respective Riedel shear zones. This review of the 2020 M_w6.6 Masbate earthquake reveals new insights into the seismic hazard and seismotectonic setting of Masbate province in Central Philippines.

1 Introduction

A M_w6.6 earthquake jolted the island of Masbate on the 18th of August 2020, and was followed by a strong aftershock in about 10 minutes (Aurelio et al., 2021). In the span of 32 hours after the mainshock, 244 aftershocks were recorded ranging from M1.6 to M5.1 (PHIVOLCS, 2020). The focal mechanism solution of the mainshock illustrates a strike-slip movement with epicenter at 7 km S29°E of Cataingan, and a depth of 21 km (PHIVOLCS, 2020). The earthquake resulted in devastating losses in terms of human lives and properties (NDRRMC, 2020). The heavy impacts of the earthquake warrants a thorough evaluation of the event to support the assessment of seismic hazards to mitigate losses and damages for the next earthquakes in the island of Masbate.

Preliminary assessments using Sentinel-1 descending track interferograms show butterfly fringes and phase shifts between 3 to 30 cm along the line-of-sight (LOS) (PHIVOLCS, 2020) and >15 cm ground deformation along the ascending track (Tiongson and Ramirez, 2022). The ascending interferograms used a 12-day (15-27 Aug. 2020) temporal baseline, indicating the combination of coseismic and post-seismic slip components alongside the reduced coherence due to the interval. Spectral

https://doi.org/10.5194/egusphere-2023-978
Preprint. Discussion started: 22 June 2023

analysis (Simborio et al., 2022) outlined a 3.0 km/s rupture velocity beginning on a shallow region of the southern fault plane with peak ground displacements ≥1.0 m. The InSAR and seismological models underestimate and overestimate the slip, respectively, compared to the seismic moment (Wells and Coppersmith, 1994).

This study provides first-order measurements of the coseismic surface offsets using the novel optical image correlation (OIC) and the post-seismic deformation using time-series InSAR analysis. The application of OIC in the Philippines is introduced to highlight its importance when used alongside interferometry. The simultaneous application of OIC and InSAR provides complementary information on the decorrelated portions of the coseismic interferogram to improve the understanding of the 2020 M_w6.6 Masbate earthquake since the event is still relatively unstudied relative to the 2003 event (Besana and Ando, 2005; Lai et al., 2019; Tsutsumi and Perez, 2011, 2013). The acquired slip distributions offer new information on the seismotectonics of Masbate, which is critical to assess consequent seismic hazards. Finally, remote sensing data are coupled with morphological interpretations of observed surface ruptures to accentuate the stress regime that operates in Masbate, expanding upon the known structural characteristics of the central Philippines.

2 Geologic Setting and Tectonic Framework

The Philippines is a region of active tectonics and volcanism arising from the interaction of the Sunda Block of the Eurasian Plate, and the Philippine Sea Plate (Aurelio, 2000a; Bird, 2003) (Fig. 1a). Oppositely dipping subduction margins flank the archipelago: the east-dipping Manila, Sulu, Negros, and Cotabato Trenches in the west; and the west-dipping Philippine Trench and East Luzon Trough in the east (Aurelio, 2000a; Barrier et al., 1991). The eastern margin accommodates the northwesterly advance of the Philippine Sea Plate at a rate of 3-9 cm yr^{-1} relative to the Eurasian Plate (Seno, 1977), while the western end consumes the subducting Sunda Block moving at a rate of 10 mm yr^{-1} eastward relative to the Eurasian Plate (Chamot-Rooke and Le Pichon, 1999). The interaction and oblique convergence of the tectonic plates that bind the country resulted in the formation of the approximately 1,200 km long sinistral Philippine Fault (PF) in the Middle Miocene (Allen, 1962; Fitch, 1972; Tsutsumi and Perez, 2013; Pinet and Stephan, 1990) as the Philippine Sea Plate's motion shifted counterclockwise from northward to a northwestward direction (Aurelio, 2000a). An ASEAN-wide GPS network assessment (Aurelio et al., 1997; Aurelio, 1998, 2000b; Rangin et al., 1999) corroborated an extant 2-3 cm yr^{-1} slip rate throughout the fault zone. An approximately 580 km northeast convex section of the PF traverses the central Philippines from the southeastern portion of Quezon province to Leyte island (Fig. 1b). Coined the Philippine Fault Bend, the deformation zone in the midsection of the PF is characterized by a N50°W fault strike and forms a releasing bend structure relative to the approximately N20°W general strike north and south of the central section (Lagmay et al., 2005).

2.1 Geology of Masbate

The PF and Sibuyan Sea Fault (SSF) are the prominent structural features in the Masbate island (PHIVOLCS, 2020; Tsutsumi and Perez, 2013) (Fig. 1b). The Masbate segment extends from Burias and Ticao islands in the north, and strikes N40°W as it crosses the southeastern tip of the mainland (Aurelio et al., 1991). In terms of morphology, it spans approximately 30 km along

https://doi.org/10.5194/egusphere-2023-978
Preprint. Discussion started: 22 June 2023

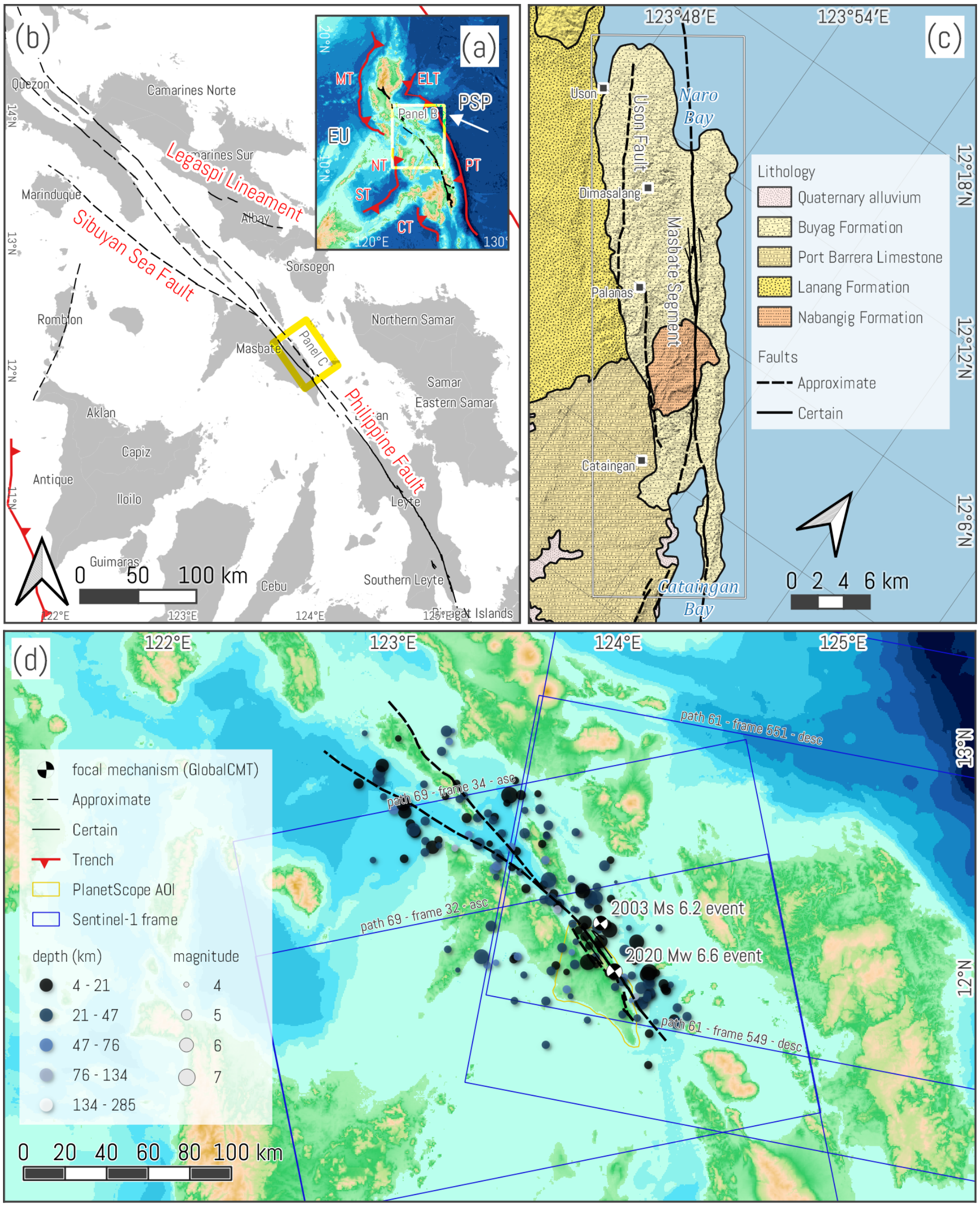

Figure 1. A) Regional geologic setting of the Philippine archipelago showing the adjacent Philippine Sea Plate (PSP) and Eurasian Plate (EU). The large-scale tectonic features are also depicted, including the east-dipping subduction zones - the Manila Trench (MT), Negros Trench (NT), Cotabato Trench (CT), and Sulu Trench (ST) on the western side; west-dipping trenches - East Luzon Trough (ELT) and Philippine Trench (PT) on the eastern side; and the resultant Philippine Fault running across the archipelago. White arrow indicates the movement direction of the Philippine Sea Plate. B) Major structural features directly affecting Masbate including the central Philippine Fault Zone (Guinayangan, Masbate, and Leyte segments), their approximate offshore projections, the Legaspi Lineament, and the Sibuyan Sea Fault. C) Southeastern Masbate area showing the involved lithologic units and traces of the Philippine Fault and Uson Fault. Black-white bounding box highlights the primary region of interest. Bathymetry data from GEBCO. Lithology adapted from Manalo et al. (2015). Trace of active structural features adapted from PHIVOLCS. D) Historical seismicity of the Masbate island from 1917 to 2022 showing the moderate earthquake centers (M4∼6.6) with focal mechanism solutions of the February 2003 and August 2020 events. Background topography and bathymetry from GEBCO. Earthquake centers acquired from USGS-NEIC. Focal mechanism solutions sourced from GlobalCMT.

https://doi.org/10.5194/egusphere-2023-978
Preprint. Discussion started: 22 June 2023

a linear trough parallel to the coastline (PHIVOLCS, 2020; Tsutsumi and Perez, 2013). Complexities in the fault geometry include an approximately 400 m narrow stepover, delineated between 12°08’ N and 12°06’ N latitude, and a bifurcation around 12°03’ N. The northeastern leg of the bifurcated structure has a northeast convex trace at 12° N and connects to the Leyte segment, whereas the southwestern leg strikes at N20°W and appears to terminate at Cataingan Bay (PHIVOLCS, 2018). Offshore seismic profiling in the bay (Llamas and Marfito, 2022) show left-stepping faults and negative flower structures that denote transtensional deformation in the region.

The SSF is another sinistral strike-slip fault with a normal component (Aurelio et al., 1991; Bischke et al., 1988). It runs parallel to the PF in mainland Masbate then deflects westward into the Sibuyan Sea (Fig. 1b). The extension component associated with the SSF is represented by tilted blocks formed from normal faulting and bathymetric depressions in the Sibuyan Sea (Bischke et al., 1990). The SSF alters the stress regime in Masbate and is manifested as extensive and compressive structures in seismic profiles between the junction of the SSF and PF (Aurelio et al., 1997). The SSF was also described as separate from the PF and is a manifestation the transtensional deformation with the $\sigma 3$ oriented perpendicular to the PF (Aurelio, 1992; Aurelio et al., 1991). GPS measurements further substantiate this regime on the local scale (Bacolcol, 2003; Duquesnoy et al., 1994).

Ophiolites comprise the basement complex of Masbate island and are unconformably overlain by a series of sedimentary and igneous units (Fig. 1c). The Cretaceous Panguiranan Chert represents the pelagic cover of the ophiolite sequence (Aurelio and Peña, 2010). The Late Oligocene Nabangig Formation is the oldest lithologic unit underlying the area of interest and is composed of a clastic sequence with recrystallized limestone. The Middle Miocene Lanang Formation lies unconformably over the Nabangig Formation, and consists of highly deformed sedimentary rocks ranging from conglomerates to mudstones (Manalo et al., 2015). Majority of the study area is underlain by the Miocene-Pliocene Buyag Formation. It overlies the Lanang Formation and is composed of conglomerates with fine-grained igneous clasts and interbedded shale and siliceous sediments. The largely coralline Pleistocene Port Barrera Limestone is the youngest stratigraphic unit in the province (Porth et al., 1989).

2.2 Seismotectonics of the Masbate Segment

Bacolcol (2003) and Lai et al. (2019) described the Masbate segment as the transition zone between the northern and southern segments of the central PF. Historical earthquake information revealed recurrence intervals of as short as five years (Besana and Ando, 2005) for moderate magnitude (M5.5~6.2) earthquakes to as much as 238 years using slip deficit rates between the 2003 event and interseismic velocities (Lai et al., 2019). A marked absence of strong events beyond M>7.0 in the past four centuries is also apparent (Bautista and Oike, 2000; SEASEE, 1985). A map (Fig. 1d) of moderate seismicity between 1917 and 2022 culled from the United States Geological Service - National Earthquake Information Center (USGS-NEIC) highlights the earthquake centers related to the Masbate segment and the SSF during this period. Observations and discussions on the 2003 event led Besana and Ando (2005) to characterize the seismic activity of the segment as capable of generating moderate to large events that produce ruptures larger than expected and can be succeeded by post-seismic deformation or creep.

The 2003 M_s6.2 event is the previous notable earthquake in the province that produced an approximately 20 km long rupture with epicenter in the northern portion of the Masbate segment. It was accompanied by either post-seismic deformation or a slow creep component (Besana and Ando, 2005; Lai et al., 2019; Tsutsumi and Perez, 2011, 2013). Kinematic offsets were

https://doi.org/10.5194/egusphere-2023-978
Preprint. Discussion started: 22 June 2023

measured at a maximum of 47 to 50 cm, which is beyond the expected peak offsets for a $M6.2$ earthquake, based on empirical magnitude scaling equations (Wells and Coppersmith, 1994). Lai et al. (2019) attributed the post-seismic deformation to the significant excess moment released by the earthquake. Aftershock analysis of earthquakes within two months of the 2003 temblor showed a cluster of $M5.0$-6.0 epicenters at the southern portion of the fault. The aftershocks were accompanied by the development of hairline fractures near Cataingan that expanded to as much as 8 mm (Besana and Ando, 2005). In addition, Bacolcol et al. (2005) recorded 10 cm GPS deviations within six months after the mainshock, supporting observations of post-seismic deformation. Coulomb stress transfer (CST) analysis showed that the 2003 event raised the stress in the southern part of Masbate by approximately 0.3 to 1 bar (Legaspi et al., 2018), which is presumed to cause the 2020 moderate earthquake along this segment.

The apparent absence of strong earthquakes ($M>7.0$) in the Masbate segment may be explained by the presence of creep (Scholz, 1998). Aseismic slip during interseismic periods was measured at 2.3 ± 1.1 cm yr^{-1} through GPS (Bacolcol et al., 2005) and 0.7-1.7 cm yr^{-1} through alignment arrays (Tsutsumi et al., 2016). A moderate background seismicity can be observed along the Masbate segment (Fig. 1d) and is further described in PHIVOLCS reports (1999).

3 Data and Methods

The ground motion components of the Masbate earthquake were measured using optical and radar satellite data. Pixel offset tracking on PlanetLabs image pairs was accomplished using the `mm2dpossism` binary of the MicMac program (Rosu et al., 2015) for the horizontal coseismic displacements. Interferometric Synthetic Aperture Radar (InSAR) was done using the European Space Agency's (ESA) Sentinel-1A and 1B radar data with a 6-day temporal baseline for the coseismic slip and a 31-day time series after the mainshock for the post-seismic deformation following the rapid aftershock decay duration (this study). Corresponding slip information was used for the detailed observation and analysis of the ground deformation caused by the 2020 Masbate earthquake event.

3.1 Spatiotemporal Seismicity Analysis

Earthquake data from 2019 to 2021 with magnitudes $M\geq1.0$ were gathered from the PHIVOLCS online earthquake archive. Foreshock and aftershock patterns were analyzed by plotting the distribution of both magnitude and frequency in time and space. All seismicity information was primarily used to define the earthquake periods (Farrell et al., 2009; Mogi, 1963) related to the 2020 Masbate event. Focal mechanism solutions acquired from PHIVOLCS, USGS, and GlobalCMT were used for the analysis of the nodal planes present in the double-couple as a seismological basis of the sense of movement of the fault plane responsible for the mainshock.

3.2 Optical Image Correlation

PlanetScope satellite imagery (Planet Team, 2017–) was the primary dataset due to the daily data acquisition and high spatial resolution of available products. Images with the least cloud cover covering the region of interest (Fig. 1c) with a maximum

https://doi.org/10.5194/egusphere-2023-978
Preprint. Discussion started: 22 June 2023

Table 1. Satellite geometry and acquisition parameters of the PlanetScope data used in the study. Values of the satellite azimuth (satAzi) are unavailable for the older images in the table. Available tiles for 23 June 2020 are merged to create a single mosaic to maximize the extent. The two datasets for 2 April 2020 are analyzed separately.

Acquisition	satID	satAzi	view∡	sunAzi	sunElev
2019-11-28T01:53:43	103e	-	1.2	143.9	48.7
2020-04-09T00:33:57	100d	-	0	90.3	42.7
2020-04-17T02:35:36	106e	-	2.1	92.5	73.1
2020-06-06T00:26:15	0f32	-	3	69.9	41.8
2020-06-23T01:29:47	2263	272.7	2	66.4	55.4
2020-06-23T01:54:27	100a	102.6	1	63.2	61.1
2020-07-07T00:19:38	1048	204.5	0.1	70.4	39.2
2020-11-18T02:03:10	105c	98.7	5	146.2	52.6
2020-11-29T01:51:59	1010	98.0	5	143.8	48.8
2020-12-24T02:21:12	1069	261.0	3	149.9	49.4
2021-04-01T02:16:14	241c	99.1	2	106.1	66.2
2021-04-02T02:13:12	1105	168.7	0.1	104.3	65.6
2021-04-02T01:54:40	1013	276.8	5	101.2	60.8
2021-04-11T01:33:11	2276	98.6	4.1	93.2	57.7
2021-04-12T02:15:35	227c	98.4	4.9	96.1	68.1
2021-06-05T01:51:14	1038	98.2	4.9	63.9	61.7
2021-06-10T23:23:03	1049	84.5	3	70	27.5
2021-07-08T02:15:18	2274	12.8	0.2	61.7	65.1
2021-07-11T01:26:43	2434	277.1	5	68.8	54.1

15 % obstruction threshold were selected. Ortho Tile products with a 3.125 m ground resolution, processed at level 3A and corrected for surface reflectance (SR) were utilized. When Ortho Tile products were unavailable, we used Ortho Scene products downsampled to 3.125 m ground resolution and corrected for top-of-atmosphere (TOA) reflectance.

To observe the influence of time on the quality of the output offset rasters, two sets of temporal ranges were tested for the Masbate event (Fig. 2). Five short-term pairs were selected from visually feasible images sampled months apart in 2020, whereas ten *annual* pairs were roughly one year apart (Table 1). This was done to minimize the effect of environmental variables following the approach of Elliott et al. (2020a).

The image pairs were coregistered to a Sentinel-2 basemap using the global coregistration function of the Automated and Robust Open-Source Image Co-Registration Software (AROSICS) (Scheffler et al., 2017) to increase the registration accuracy while preserving the deformation signal. The pairs were clipped to their overlapping extents with a Universal Transverse

https://doi.org/10.5194/egusphere-2023-978
Preprint. Discussion started: 22 June 2023

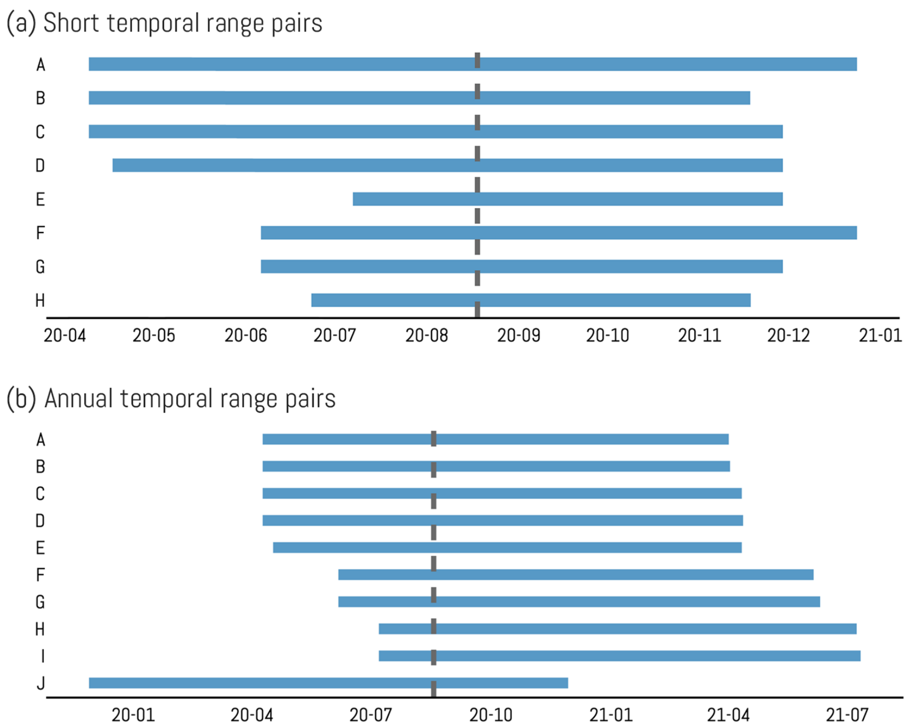

Figure 2. Two classes of Planet satellite imagery pairs evaluated through optical correlation. A) short-term pairs taken within the same year as the Masbate earthquake ranging from five to nine months apart and as close to the event as possible. B) Approximately annual span pairs acquired at about 365 days apart where environmental interference is expected to be at a minimum (Elliott et al., 2020a).

Mercator (UTM) projection and either 8- or 16-bit integer pixel data type as required by MicMac. Manual cloud masking was accomplished using the `saisiemasqQT` binary of MicMac for precision masking.

Correlations in the spatial domain were performed with MicMac on the prepared image pairs using the following parameters:

– 7x7 window size (`SzW=3`) for a 21.875 m search grid on each side to compensate for feature-related noise and expected displacement,

– 0.5 regularization factor (`Reg=0.5`) to provide distance-based correlation weights on the neighboring pixels within the window for noise reduction, and,

– pixel subsampling parameter of 2 (`SsResolOpt=2`) as recommended by Canizares et al. (2020) for earthquake events to resolve displacement fields close to the ground resolution of the source imagery.

The resulting output files were georeferenced using `gdal_translate` with the `-a_ullr` flag (GDAL/OGR contributors, 2021) to ensure a 1:1 alignment with the input image pairs without warping the rasters. To retain most deformation signals, the correlation threshold was set to 50 %. A non-local median (NLM) filter with a low H-noise value was applied to prevent

https://doi.org/10.5194/egusphere-2023-978
Preprint. Discussion started: 22 June 2023

flattening real ground deformation signals while improving the signal-to-noise ratio (SNR). The outputs were then translated into the spatial domain by multiplying the rasters with the ground resolution of the input files. Primary offset rasters subjected to profiling was selected based on noise levels, atmospheric obstruction, pre-processing accuracy, ROI coverage, and quality of slip visualization.

The post-processed data generated coherent offset maps along the N-S ($D_{N_{OIC}}$) and E-W ($D_{E_{OIC}}$) horizontal axes with a 3.125 m pixel resolution. Slip measurements with respect to the general fault strike azimuth (θ = 325°) of the Masbate segment were acquired by transposing the N-S and E-W slip into fault-oriented components using the following equations (Elliott et al., 2020a):

$$D_{\parallel} = D_{N_{OIC}} \cdot \cos(\theta) + D_{E_{OIC}} \cdot \sin(\theta) \quad (1)$$

$$D_{\perp} = D_{N_{OIC}} \cdot \sin(\theta) - D_{E_{OIC}} \cdot \cos(\theta) \quad (2)$$

The fault-parallel ($D_{\parallel}$) direction refers to movements parallel to the fault trace represented by laterally offset features on the field. This component was the sole subject of profiling due to the stronger horizontal offset signal in the field. The tension-compression ($D_{\perp}$) aspect detectable from the fault-normal component was not analyzed due to the minimal deformation along the vertical axis, further complicated by high noise amplitudes.

Wide swath profiles (321 x 161 px, roughly ~1.0 x ~0.5 km) along the fault trace were measured with StackProf (Delorme, 2021) developed for the MicMac project. The slip values from profiles aided the measurement of the near-fault slip distribution for comparison with offsets measured in the field. The offsets were calculated from the intercepts of the regression of median displacements, excluding the apparent noise signals and zero correlation pixels to highlight the genuine earthquake slip in the arctangent model. Validated slip data were plotted along the fault strike to show the spatial trends. Absolute standard deviations on the eastern and western fault blocks represent the measurement uncertainties in individual box profiles. Slip uncertainties represented by the standard error of intercepts of the regression lines for the east and western fault blocks were calculated automatically using StackProf. The coseismic displacement curve was calculated using a weighted moving mean approach with minimal smoothing to prevent the removal of small deviations along the strike.

3.3 Small Baseline Subset (SBAS) Interferometry

Coseismic and post-seismic interferograms were processed with NASA's Alaska Satellite Facility Distributed Active Archive Center (ASF DAAC) Hybrid Pluggable Processing Pipeline (HyP3) (Kennedy et al., 2021). Sentinel-1A/B single look complex (SLC) C-band radar data acquired through the interferometric wide (IW) swath mode was used. Data with 6 to 12-day intervals from paths 61 (descending track) and 69 (ascending track) (Fig. 1d) imaged between 14 to 21 August 2020 for the coseismic slip and 20 August to 20 September 2020 for the afterslip were multilooked by 20 in the azimuth direction and 4 in the range resulting to a pixel size of 80 x 80 m to minimize the effect of land cover (Table 2).

https://doi.org/10.5194/egusphere-2023-978
Preprint. Discussion started: 22 June 2023

Table 2. Summary of reference and secondary granules processed within Alaska Satellite Facility's Hyp3 processor to create interferograms.

Track	Reference	Path/Frame$_1$	Secondary	Path/Frame$_2$	Perp. baseline (m)	Interval(days)	Stage
desc	20200814	61/551	20200820	61/549	-76.4	6	co
asc	20200815	69/32	20200821	69/34	107.1	6	co
desc	20200820	61/549	20200901	61/549	50.4	12	post
asc	20200821	69/34	20200827	69/32	-173.3	6	post
desc	20200826	61/551	20200901	61/549	-76.4	6	post
asc	20200827	69/32	20200902	69/34	126.0	6	post
asc	20200827	69/32	20200908	69/32	42.6	12	post
desc	20200901	61/549	20200907	61/551	49.6	6	post
desc	20200901	61/549	20200913	61/549	68.5	12	post
asc	20200902	69/34	20200908	69/32	-83.1	6	post
asc	20200908	69/32	20200920	69/32	49.9	12	post
desc	20200913	61/549	20200919	61/551	-39.4	6	post

Small baseline time series analysis (SBAS) was employed using MintPy (Yunjun et al., 2019) to quantify the post-seismic deformation in the aftershock observation period. Atmospheric corrections were not applied, since the study area is highly localized relative to the global dataset implemented in available databases. Furthermore, the unwrapping reference point was set to a common high coherence pixel for both tracks. The ascending (V_A) and descending (V_D) LOS velocities were projected into the azimuthal fault strike ($\theta = 325°$) (Dianala et al., 2020; Lindsey et al., 2014; Tymofyeyeva and Fialko, 2018) to estimate the fault-parallel ($V_{||}$) and vertical (V_Z) post-seismic velocities. The approach assumes a zero third component acceptable for areas of relatively simple faulting. Equation 3 was used to derive the fault-oriented afterslip LOS velocities within the `asc_desc2horz_vert` script in MintPy. The pixel unit vector directed to the satellite was decomposed into e, n, and u representing the east, north, and upward directions of both tracks, respectively.

$$\begin{bmatrix} V_A \\ V_D \end{bmatrix} = \begin{bmatrix} e_A \sin(\theta) + n_A \cos(\theta) & u_A \\ e_D \sin(\theta) + n_D \cos(\theta) & u_D \end{bmatrix} \begin{bmatrix} V_{||} \\ V_Z \end{bmatrix} \tag{3}$$

The total afterslip was obtained by multiplying the fault-parallel component with the temporal range of the time series and smoothed the data using an NLM filter to arrest pixel outliers. Swath profiles (Krambach, 2015) were taken at 0.5 km intervals with a 3.5 km swath width across the fault strike. Slip error estimates come from the sum of the standard error of regression intercept on both sides of the fault, following the StackProf approach (Delorme, 2021). The spatial distribution of afterslip along the strike was evaluated by applying a low smoothing factor on the moving mean displacement curve. The vertical post-seismic displacement was not investigated due to the primarily horizontal ground movement. The coseismic interferogram

https://doi.org/10.5194/egusphere-2023-978
Preprint. Discussion started: 22 June 2023

was qualitatively compared with the optical correlation data due to the lack of resolvable slip in the near-fault region due to decorrelation.

3.4 Ground Truthing

Field investigation was conducted from 18 to 21 May 2022 to identify and measure the horizontal offsets of the ground rupture. Locations of known ground rupture (dela Cruz, per. comm., 2022) were complemented by points of interest identified from the image correlation outputs and InSAR. Significant contrast on the horizontal offset rasters on the approximate and certain fault traces was the primary criterion to select the points of interest for field checking. Observation points with measurable feature offset and ruptures were plotted along the strike to show the attitude and slip distribution along the fault. The measured horizontal offsets were used to validate the results of the remote sensing analysis. Finally, the surface rupture length, and maximum and average displacements were derived from the conjoined remote sensing outputs and field data to estimate the seismic moment.

4 Results

4.1 Seismicity

4.1.1 Earthquake Frequency and Temporal Relationships

The frequency-time distribution plot of hypocenters between 25 August 2019 to 18 August 2021 shows the immediate seismicity related to the 18 August 2020 M_w6.6 event (Fig. 3). The foreshocks, mainshock, and aftershocks are identifiable in the probability density subplot (Fig. 3a) as a distinct bell-shaped curve relative to the generally quiescent background activity. The typical daily earthquake activity of Masbate island is less than ten events per day, corresponding to moderate background seismicity with multiple days without recorded earthquake activity. The increasing earthquake frequency defines the foreshock sequence in the probability density subplot (Farrell et al., 2009) that began 32 days before the mainshock. The peaks correspond to 141 earthquakes which were mostly aftershocks on 18 August 2020. A negative slope in the probability density subplot depicts the aftershock sequence. The decaying earthquake frequency is initially symmetrical to the foreshock trend with an inflection point around 30 days after the mainshock, which then transitioned to a more gradual decrease. The aftershocks persisted for 166 days or up to 31 January 2021. Succeeding return to background levels is characterized by low seismic activity and days without earthquakes are closer to each other relative to the background activity from 2019 to early 2020.

4.1.2 Spatiotemporal Earthquake Distribution

In general, the background seismicity ($M \leq 4$) is well distributed throughout the overall length of the Masbate segment of the PF traversing the islands of Ticao, Burias, and the provincial mainland (Fig. 4a). However, an absence of seismic activity is noticeable in the northern portion of the fault in mainland Masbate during this period. On the contrary, an earthquake

https://doi.org/10.5194/egusphere-2023-978
Preprint. Discussion started: 22 June 2023

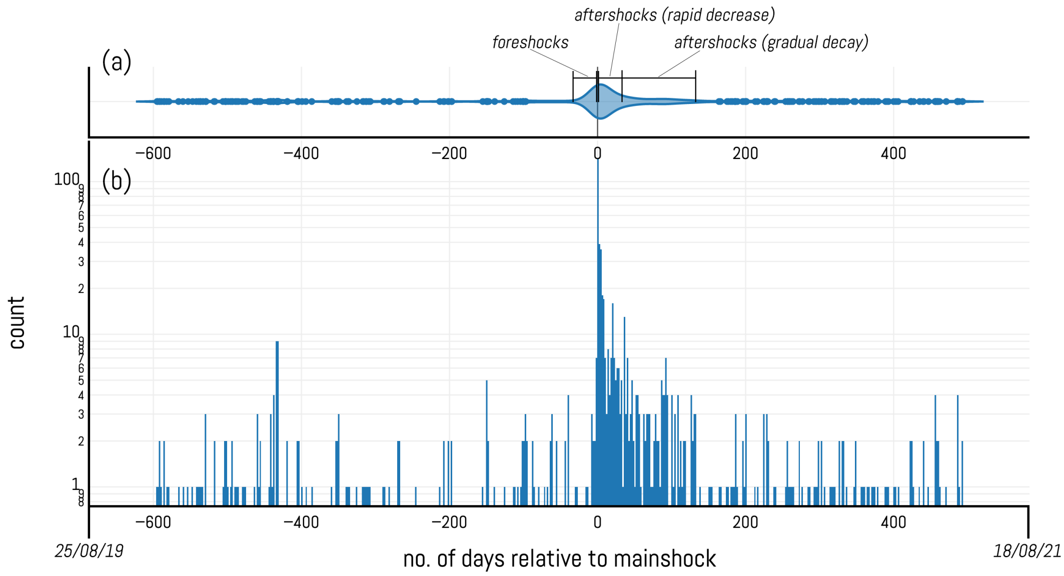

Figure 3. A) Earthquake probability density subplot showing the normalized population of earthquakes per day, highlighting the contrast between the periods of the earthquake sequence. B) Plot showing the number of earthquakes with magnitudes $M \geq 1$ related to the Masbate segment and their temporal distribution relative to the 18 August 2020 mainshock.

Table 3. Fault mechanism parameters from PHIVOLCS, USGS, and GlobalCMT for the M_w6.6 Masbate earthquake mainshock on 18 August 2020.

Source	**Time**	**Long**	**Lat**	**Depth**	**Nodal plane 1**			**Nodal plane 2**		
	(UTC)	(° E)	(° N)	(km)	Str	Dip	Rake	Str	Dip	Rake
PHIVOLCS	00:03:00	124.00	12.00	5	235°	64°	-174°	142°	85°	-26°
USGS	00:03:48	124.13	12.03	10	231°	86°	167°	322°	77°	4°
GlobalCMT	00:03:53	123.98	12.04	12	233°	89°	177°	323°	87°	1°

cluster occurred near the location of the mainshock. Foreshock activity is concentrated in southeastern Masbate adjacent to the mainshock and is composed of mostly weak ($M2\sim3$) and shallow hypocenters peaking at M4.9 (Fig. 4b).

Three (3) moment tensor solutions from GlobalCMT, PHIVOLCS, and USGS highlight the mainshock's dominant left-lateral strike-slip motion (Fig. 4c; Table 3). The solutions of PHIVOLCS and USGS show a noticeable, albeit minimal, dip-slip component towards the NNE. The epicentral location of the mainshock from GlobalCMT and PHIVOLCS coincided with the fault trace, while USGS' focal mechanism solution deviated to the northeast of the fault.

Aftershocks that transpired on the same day as the mainshock (Fig. 4d) are shallow (1-30 km) and densely grouped in the southeastern offshore extension of the segment and deepen (10-50 km) as they taper toward the onshore portion. The aftershocks have weak magnitudes ranging from M2.0 to M4.4. Succeeding first-month aftershocks are weak to moderate,

https://doi.org/10.5194/egusphere-2023-978
Preprint. Discussion started: 22 June 2023

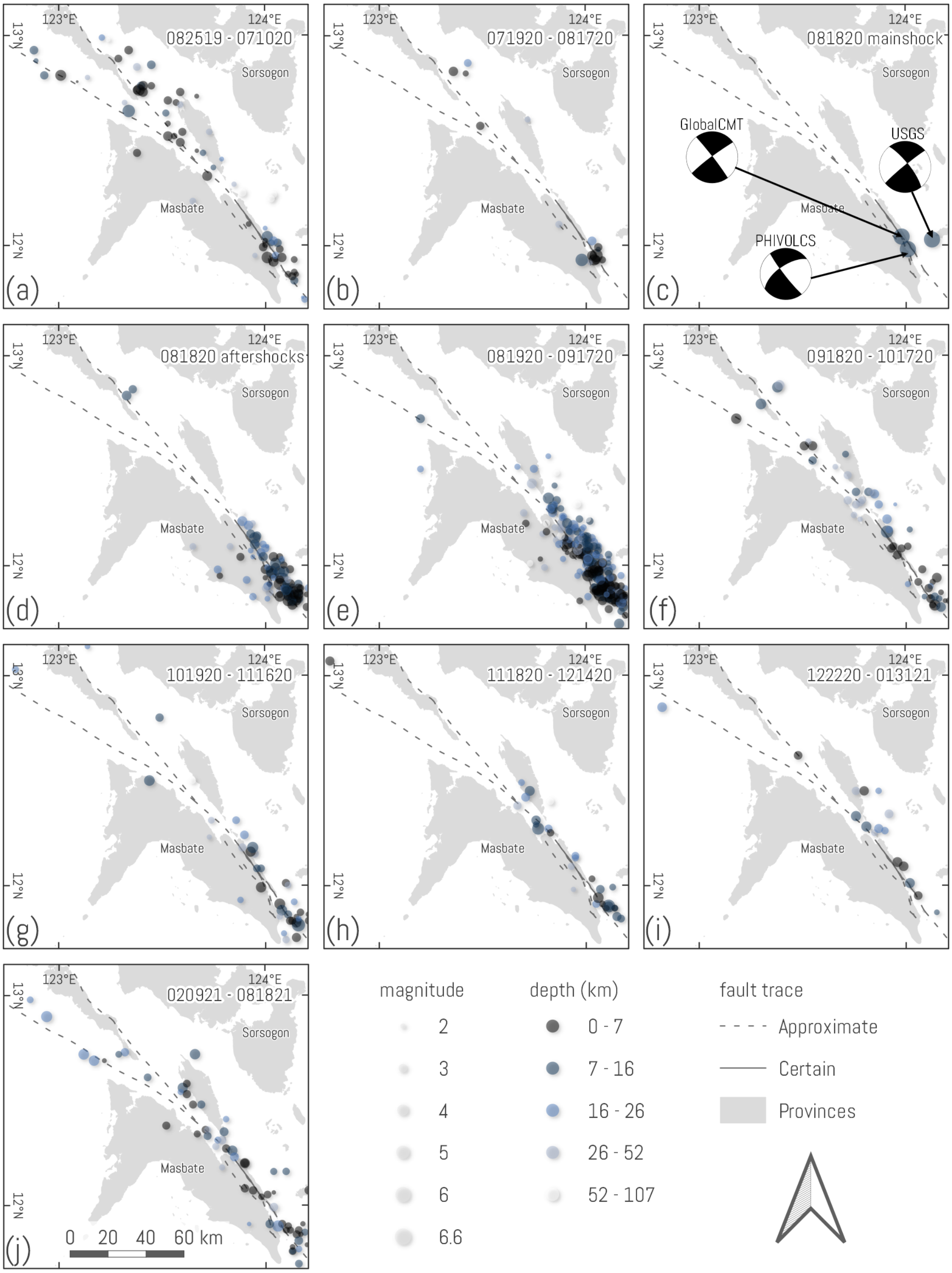

Figure 4. Spatiotemporal earthquake distribution for the Masbate segment. A) Background seismicity between 25 Aug 2019 to 10 Jul 2020. B) Foreshocks from 19 Jul to 17 Aug 2020. C) Moment tensors of the mainshock from GlobalCMT, PHIVOLCS, and USGS. D) Same-day aftershocks. E) First-month aftershocks from 19 Aug to 17 Sept 2020. F) Second-month aftershocks from 18 Sept to 17 Oct 2020. G) Third-month aftershocks from 19 Oct to 16 Nov 2020. H) Fourth-month aftershocks from 18 Nov to 14 Dec 2020. I) Last aftershocks from 22 Dec 2020 to 9 Feb 2021. J) Return to background seismicity covering 11 Feb to 18 Aug 2021.

https://doi.org/10.5194/egusphere-2023-978
Preprint. Discussion started: 22 June 2023

Table 4. Duration and date range of earthquake sequences of the 2020 Masbate event derived from the probability density plot of the frequency-time distribution. The aftershock sequence is subdivided into two following the inflection point separating the sharp and gradual decay of activity.

Sequence	Start date	End date	Duration
foreshocks	17 Jul 2020	17 Aug 2020	32 days
mainshock	18 Aug 2020	18 Aug 2020	-
aftershocks (rapid decrease)	18 Aug 2020	17 Sept 2020	30 days
aftershocks (gradual decay)	17 Sept 2020	31 Jan 2021	136 days

with a wide range of magnitudes between $M1.7$ to $M5.1$, mostly occurring at depths above 30 km. A monthly progressive dispersal of hypocenters in space is also observed, with the first month showing a dense cluster in the southeastern section that tapers to the northwest (Fig. 4e). The pattern and geographic extent of the first-month aftershocks appear to be an expansion of the same-day aftershocks. The succession of the aftershock patterns in the following months continued to scatter along the Masbate segment and the SSF while retaining a perceptible concentration in the offshore southeastern extension of the causative fault segment (Figs. 4f, 4g, 4h, and 4i). The last two months of aftershock activity (Figs. 4h and 4i) feature the least number of hypocenters throughout the aftershock sequence.

Background levels returned on 2 February 2021 defined by the well-distributed hypocenters on the fault segments with moderate magnitudes (Fig. 4j) similar to the pre-event seismicity in 2019 (Fig. 4a). The frequency and distribution of earthquakes in time and space enabled the distinction of various stages of the earthquake sequence relative to the 2020 Masbate event (Table 4).

4.2 Optical Image Correlation

4.2.1 Long and Short Temporal Baseline

The acquired optical correlation displacement maps illustrate the fault rupture and the known sinistral movement of the Masbate segment. However, high noise values tend to obscure the rupture trace. Only one of the eight image pairs from the short timespan (Figs. 2a) produced limited regions of perceptible rupture due to the low SNR. The resolved slip is comparatively clearer in the annual timespan pairs despite the persistent low SNR. The north-south slip components show better representations of the rupture, whereas the east-west components tend to be noisier. Nevertheless, the valid image pairs with resolvable displacements subjected to stack profiling exhibit reliable estimates of the slip in the near-field region.

4.2.2 Coseismic Offsets

Supplemented by the known trace of the PF from PHIVOLCS, a generalized fault trace (yellow line; Fig. 5) was delineated from the valid optical correlation displacement rasters and served as a reference for slip profiling. The fault trace is mostly

https://doi.org/10.5194/egusphere-2023-978
Preprint. Discussion started: 22 June 2023

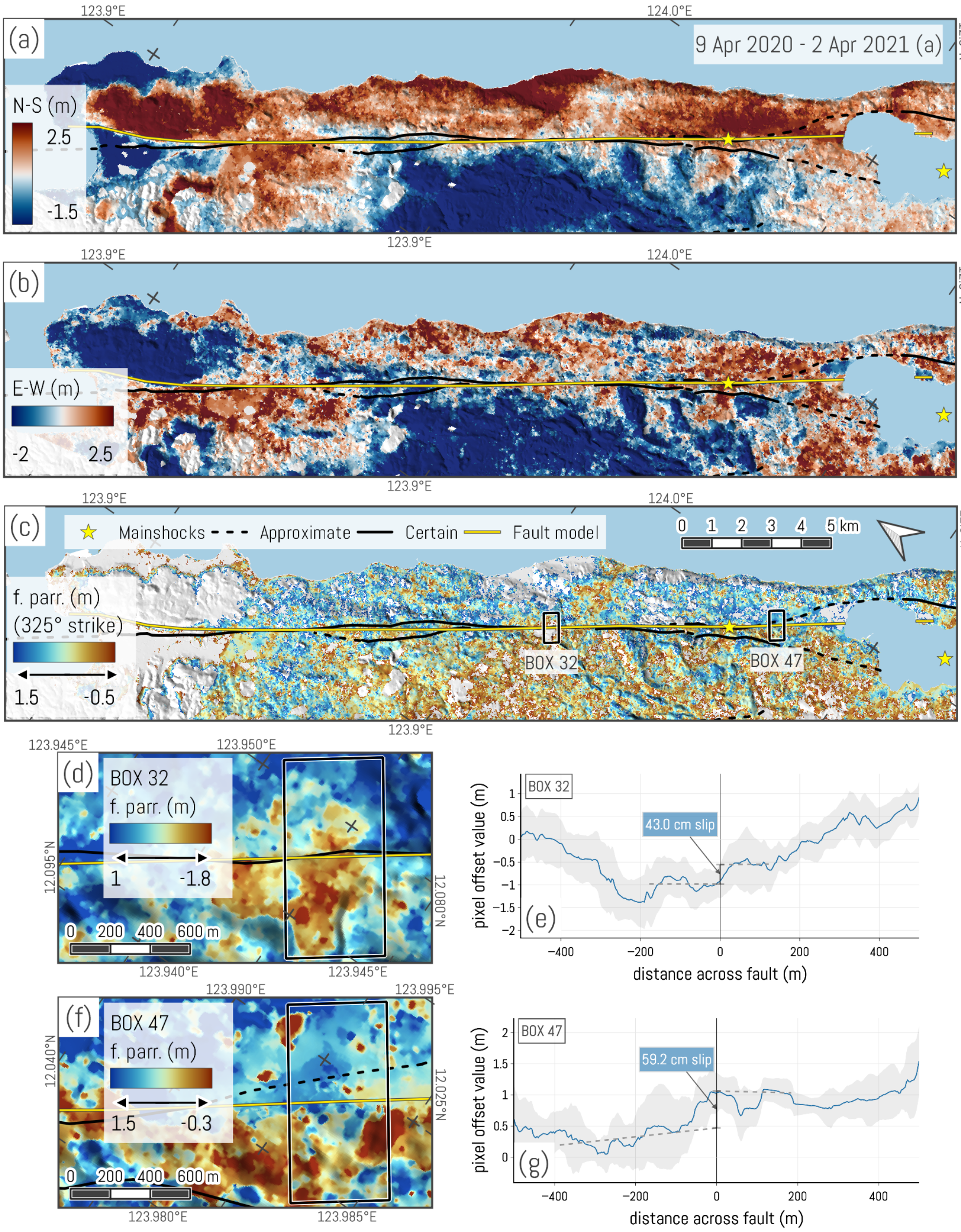

Figure 5. Optical correlation results showing the representative data from the 9 April 2020 and 2 April 2021 image pair. Blue lines in panels E and G are the absolute median fault-parallel values across the profile box. Gray shaded region in panels E and G feature the 1σ absolute standard deviation of the fault-parallel values across the fault in each box. A) N-S component. Blue refers to southward movement, while red refers to northward motion. B) E-W component. Blue refers to westward movement, while red refers to eastward motion. C) Fault-parallel component. Blue refers to movements toward the NW while red denotes motion toward the SE. D) Closer view of box 32 showing the fault-parallel offset. E) Swath profile of box 32 highlighting the 43 cm slip. Negative axis refers to the western block and vice versa. Lower regression intercept of the western block relative to the eastern block indicates sinistral movement. F) Closer view of box 47 displaying the fault-parallel offset in Cataingan. G) Swath profile of box 47 exhibiting the peak 59.2 cm sinistral offset in this particular image pair.

https://doi.org/10.5194/egusphere-2023-978
Preprint. Discussion started: 22 June 2023

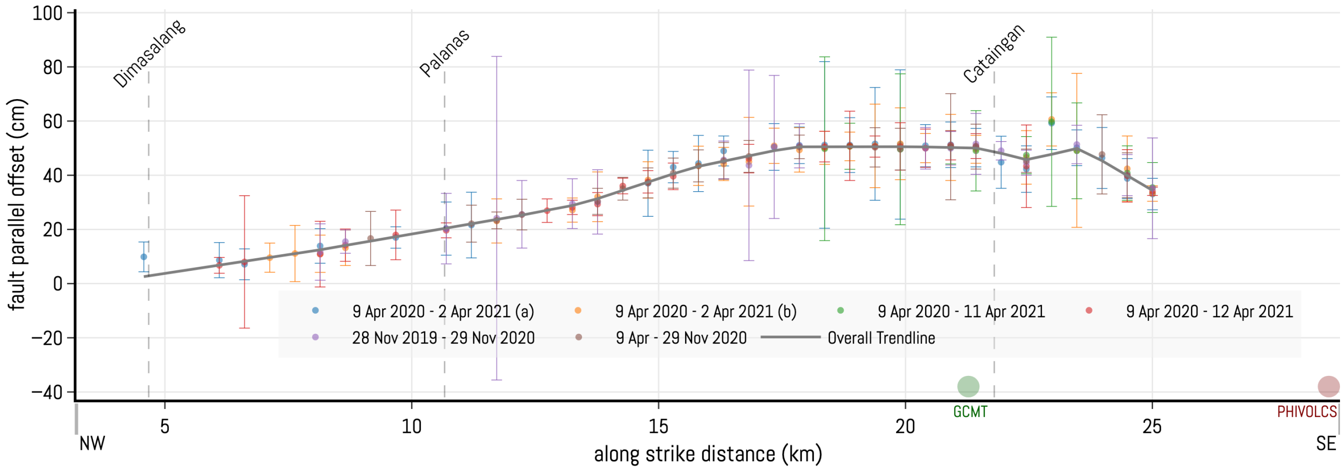

Figure 6. Along strike distribution of the fault-parallel offsets from 126 profile boxes across six image pairs. Error bars refer to the 1σ sum of standard errors of the intercepts of regressions of the east and west blocks providing slip error estimates.

straight, except for an apparent northeasterly strike rotation towards the north, where it follows the piedmont of a topographic high in Dimasalang. No measurements were acquired in the area due to anomalously high values, which are probably terrain residuals. Topographic artifacts and decreasing displacements away from the epicenter posed difficulties in delineating the northern rupture section near Naro Bay. The offset rasters show a new splay striking NW-SE that bisects the bifurcating fault trace in Cataingan, identified by PHIVOLCS (2020) and Tsutsumi and Perez (2013) in their active faults map. The rupture traverses the deltaic area and possibly continues southward across Cataingan Bay, then resurfaces on the opposite side of the bay. Smaller fractures and minute rupture components are not visible due to ubiquitous noise.

Sinistral offsets were quantified along the ~25 km onshore length of the fault from Dimasalang to Cataingan, given the inland spatial extents and continuity where optical correlation was possible. Slip measurements were not derived in the area south of the bay due to the presence of a water body, which obscured the western block and promoted edge artifacts.

Fifty-one (51) wide swath profile boxes were generated throughout the fault rupture, with the first box in Dimasalang and the last in Cataingan to determine the along-strike slip distribution (Fig. 6). The optical correlation results generated a total of 126 left-lateral measurements over six image pairs. Using a 325° general strike azimuth of the Masbate segment, the east-west and north-south displacement components (Figs. 5a and b) were transposed into the fault-parallel direction (Fig. 5c).

The 9 April 2020 - 2 April 2021 pair was selected as the representative dataset due to its wide spatial extent and reliable representation of the fault rupture. The north-south component (Fig. 5a) shows a continuous linear rupture trace from Dimasalang to the deltaic region in Cataingan, although the Dimasalang area and its border with Palanas exhibited unusually high values due to noise. The east-west component (Fig. 5b) appears less coherent, likely due to smaller ground movements in this direction or overprinting information caused by low SNR. The outputs show noise from both artificial and environmental sources, represented by topographic artifacts in the southwestern block, an apparent seamline, and reduced coherence due to differences

https://doi.org/10.5194/egusphere-2023-978
Preprint. Discussion started: 22 June 2023

in land cover between the images. Nevertheless, the fault-parallel component (Fig. 5c) show good estimates of the sinistral slip, further supported by the near-field offset models.

Box 32 (Fig. 5d), located ~6 km north of the GlobalCMT surface projection, shows a 43 cm displacement in the near-field (Fig. 5e). Pixel offset values increase in the far-field for the western block (negative x-axis), which may be due to noise. Box 47, situated ~1.5 km south of the GlobalCMT epicenter, exhibits a 59.2 cm sinistral offset. The box represents the peak offset in this image pair and displays a clear contrast between the east and western blocks despite the noise.

The plot of the slip distribution along strike (Fig. 6) displays the 126 sinistral offsets compiled from the valid offset rasters to characterize the displacement field. The slip minima are measured to range from 6 to 9 cm, located 4.5 km from the northern shoreline in Dimasalang. The displacement increased to ~50 cm around the vicinity of the GlobalCMT projection of the centroid. Slip values remained constant within a ~5 km span in Cataingan, followed by an increase to a peak ~60 cm sinistral slip. The anomaly is followed by a recession southward to the shoreline. The skewed semi-elliptical weighted moving mean curve (solid gray line; Fig. 6) yields a mean sinistral displacement of 37.7 ± 10 cm with a maximum of 60.6 ± 9.8 cm around the GlobalCMT projection of the centroid in Cataingan.

4.3 Interferometry

4.3.1 Coseismic Interferograms

The Sentinel-1 coseismic wrapped interferograms in the ascending and descending tracks (Fig. 7a and c) show the butterfly fringe pattern and oppositely directed LOS displacement vergence, which is typical of strike-slip events. The fringe lobe patterns illustrate a range increase from the ascending track and a range decrease from the descending track for the western side of the fault. Since the orbit of the ascending track is subparallel to the regional fault strike, the sinistral movement is indicated with a possible subsidence component, consistent with the moment tensor solutions (Table 3), and agrees with the sense of movement observed from the optical correlation outputs.

Low phase coherence persists in the near-fault region. Widespread decorrelation leads to mostly unusable information upon phase unwrapping due to the likelihood of creating unwrapping errors. Noise is similarly dominant and overprints most of the deformation signals in an approximately 18 km-wide region across the fault trace, hence, the lack of near-fault information in preliminary published interferograms (PHIVOLCS, 2020; Tiongson and Ramirez, 2022). In addition, the rupture is unresolved upon phase unwrapping (Fig. 7b and d) due to decorrelation. This loss of resolvable information in the near-field ultimately hinders slip measurements.

4.3.2 Post-seismic Deformation

Post-seismic interferograms capture an improved overall manifestation of the fault rupture compared to the coseismic ones (Fig. 8). This is a consequence of the expected smaller afterslip values relative to the coseismic slip, which decreases the number of fringes and increases the coherence. The temporal coverage of the interferogram stack subsequently provides a means to quantify the afterslip to complement the coseismic slip derived from optical correlation. Unwrapping errors are less frequent

https://doi.org/10.5194/egusphere-2023-978
Preprint. Discussion started: 22 June 2023

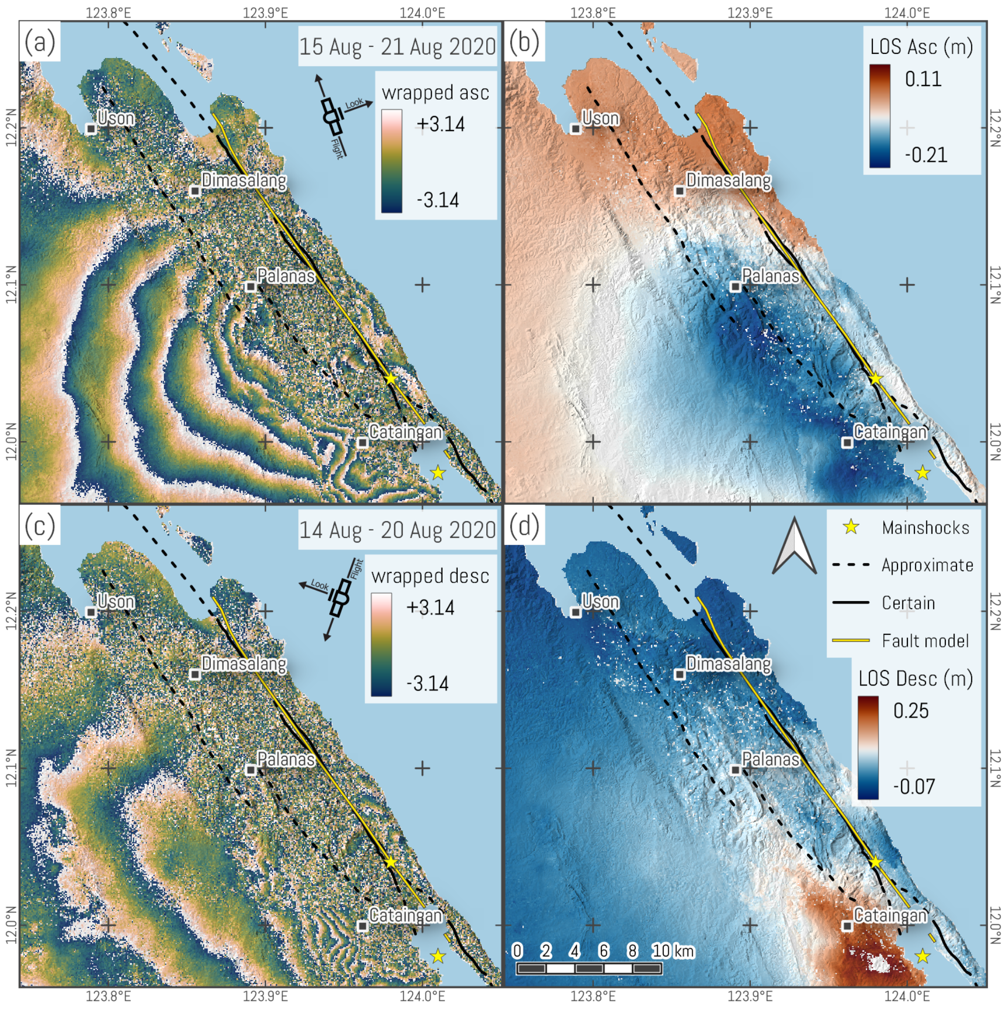

Figure 7. Sentinel-1 coseismic interferograms in ascending and descending tracks. A) Wrapped ascending interferogram. B) Unwrapped ascending track interferogram. C) Wrapped descending track interferogram. D) LOS displacement in the descending track.

https://doi.org/10.5194/egusphere-2023-978
Preprint. Discussion started: 22 June 2023

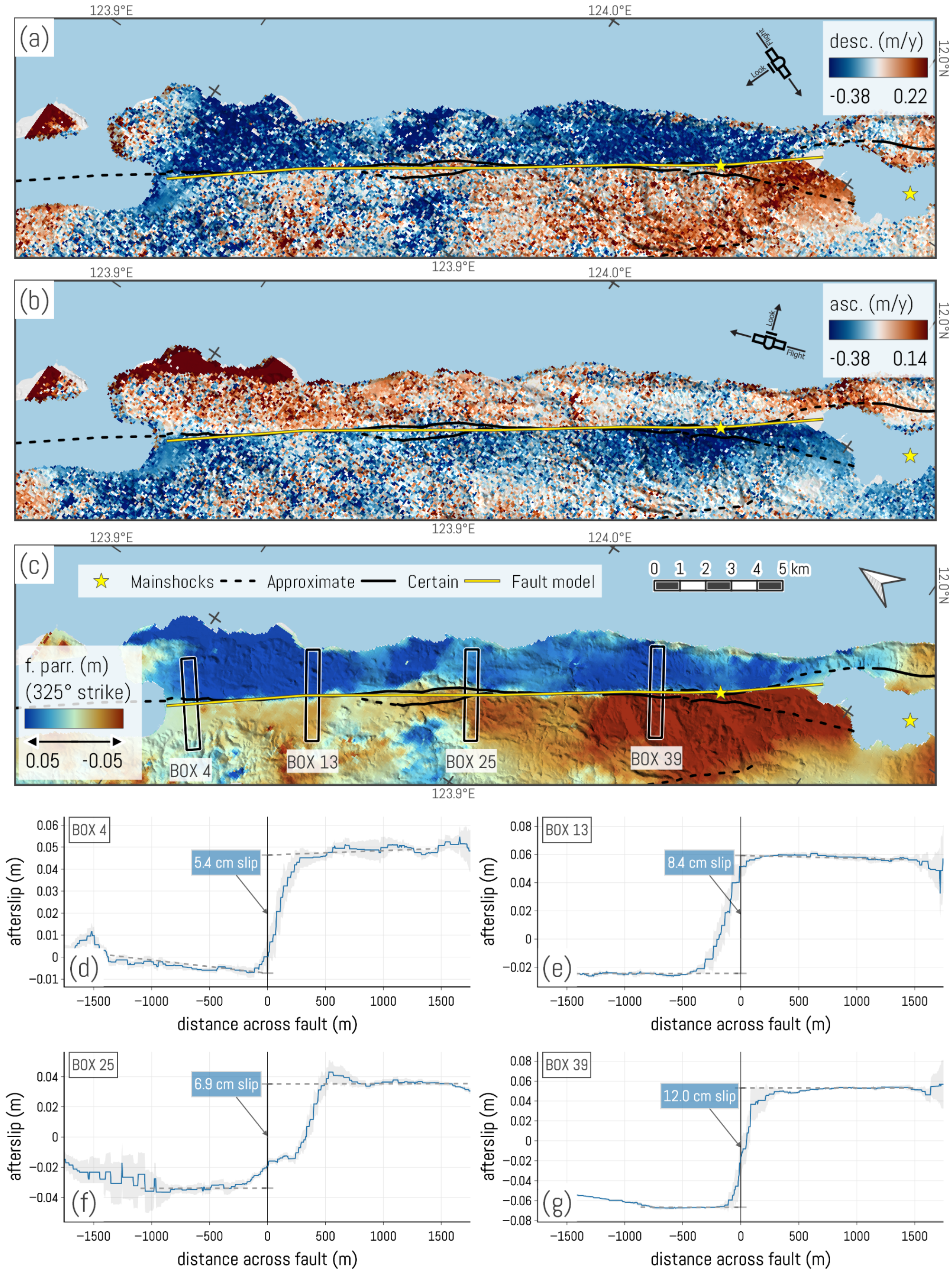

Figure 8. Post-seismic deformation between 20 August to 20 September 2020. A) Descending track time series showing range decrease (blue) and increase (red) for the eastern and western blocks, respectively. B) Ascending track time series showing range increase (red) and decrease (blue) for the eastern and western blocks, respectively. C) Projected fault-parallel post-seismic deformation field. D) Fault-parallel afterslip for box 4 in Dimasalang showing the 5.4 cm sinistral afterslip. Lower regression intercept of the western block relative to the eastern block indicates sinistral movement. Median afterslip value per pixel is shown by the blue line. Gray background exhibits the 1σ uncertainty across the box. E) Swath profile of box 13 indicating an 8.4 cm sinistral afterslip around the Dimasalang-Palanas boundary. F) Swath profile of box 25 showing a 6.9 cm afterslip in Palanas. G) Swath profile of box 39 in Cataingan showing a 12.0 cm sinistral afterslip.

https://doi.org/10.5194/egusphere-2023-978
Preprint. Discussion started: 22 June 2023

on the ascending and descending track interferograms and are further minimized upon time-series stacking. The remaining phase unwrapping errors upon stacking and filtering were manually excluded in profiling. These unwrapping errors occur as significant high amplitude phase shifts and polarity reversals, noticeable in the Dimasalang and Palanas areas.

The fault-parallel afterslip deformation field (Fig. 8c) shows a strong linear and simple fault trace that accommodated the post-seismic deformation. Deviations from the regional fault strike are observed around 5-13 km from Naro Bay in the north, represented by multiple short NNE-SSW oriented (~290-300° azimuth) bends which are adjacent to and coincide with the narrow stepover in the Palanas-Dimasalang area. However, the noticeable unwrapping errors and low ground resolution (80 m) precludes the validity and recognition of these rupture complexities.

The afterslip is measured from Naro Bay in the north towards Cataingan Bay in the south along the ~25 km simplified fault trace. Fourty-nine (49) swath profile boxes were generated along this trace. Individual afterslip measurements reveal centimetric fault-parallel afterslip with minimal across-fault variability and minor 1σ uncertainties, except where the boxes overlap with the phase unwrapping error patches. The deformation was detected up to the far-field extents of the profiles from most swath boxes.

Boxes 4, 13, 25, and 39 (Figs. 8d, e, f, and g) illustrate select wide swath profiles roughly equidistant from each other. Box 4, situated in Dimasalang, shows a 5.4 cm left lateral fault-parallel afterslip and a reasonably low variability across the fault. Unwrapping errors in the far-field at 1.5 km from the fault on both sides caused irregularities in the profile. Box 13, located around the boundary of Palanas and Dimasalang, depicts an 8.4 cm fault-parallel slip. Both sides of the fault exhibit exceedingly even slip across the fault, except for a noticeable dip in the eastern edge. The dip is likely due to data loss since the box overlapped with the water body to the east. The profile also appears to be offset by about ~100 m to the west, which corresponds to one of the abovementioned bends that may be an unwrapping artifact. Still, the measured slip from the arctangent model remains valid. Box 25 shows a 6.9 cm afterslip in Palanas, located at the southern edge of the stepover. Multiple across-fault deviations are visible around 200 and 500 m east of the fault and in the western far-field. The eastern anomalies could either be unwrapping or topography related, while the western patch comes from unwrapping issues. Box 39 in Cataingan displays a 12.0 cm sinistral afterslip with good symmetry and even across-fault distribution.

The along-strike afterslip distribution graph (Fig. 9) depicts the computed fault-parallel offsets from north to south on the mainland. The smallest value is measured in Dimasalang, adjacent to Naro Bay, amounting to 4.3 cm of sinistral afterslip. The offsets exhibit a generally increasing trend to around ~5 km from the north. Fluctuating values are observed between 6.1 to 13.8 km from the north in Dimasalang and Palanas. The measured displacements oscillate between 5.0 to 9.6 cm in this span. The increasing trend continued to a 14.3 ± 0.9 cm peak afterslip in Cataingan, located 24 km from Naro Bay and ~3 km southwest of the GlobalCMT surface projection. The displacements decrease from the maximum value to 11.5 cm on the shoreline of Cataingan Bay. The weighted moving mean curve (solid blue line) indicates a mean sinistral afterslip of 8.8 ± 0.7 cm.

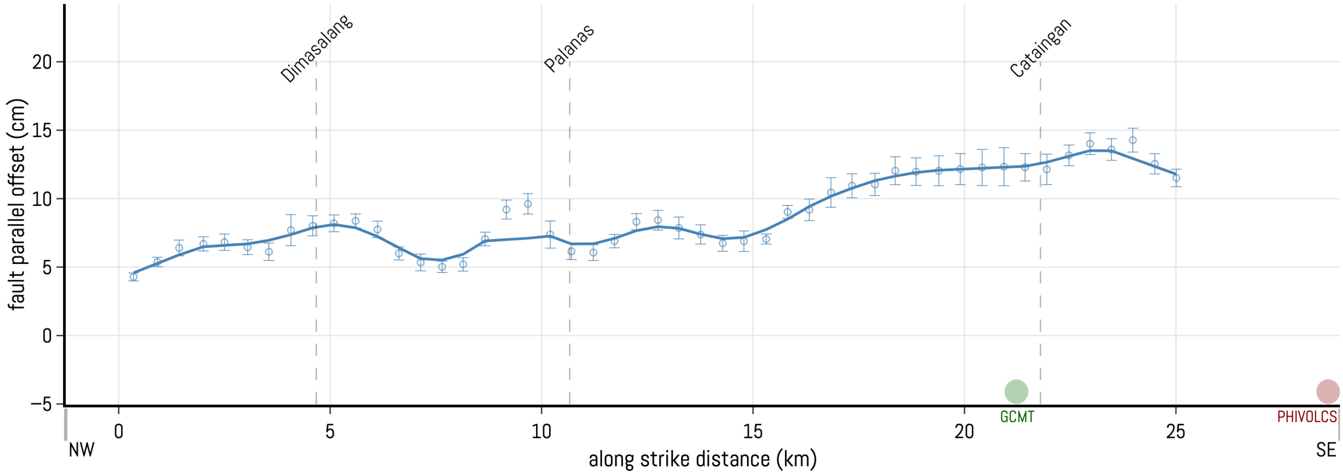

Figure 9. Along strike distribution of the fault-parallel afterslip formed by the 49 profile boxes. Error bars refer to the 1σ standard errors of the intercepts of regressions of the east and west blocks. Solid blue line shows the weighted moving mean afterslip curve.

4.4 Ground Truthing

4.4.1 Observed Surface Ruptures

Remnant earthquake effects were observed on laterally offset cultural and geomorphic features from Dimasalang to Cataingan following the known fault trace. Assisted by the remote sensing data, the observed ground manifestation of the earthquake from fifty-seven (57) stations (Fig. 10a and b) include fractures, reported earthquake-induced landslides (EIL), indications of liquefaction features and lateral spreading, secondary gravitational features, and ruptures with quantifiable displacements. Earthquake effects recorded during the field activity include reported ground shaking from interviews with locals.

The observed rupture zone of the 2020 Masbate earthquake persisted from Dimasalang to Cataingan and crossed Cataingan Bay. Measured surface ruptures strike both subparallel and at a low angle with respect to the regional fault trace (Fig. 10c) with a mean strike azimuth of 313°. The northern terminus of the surface rupture was observed on a road in Dimasalang, around ~3 km from Naro Bay, with an apparent 0.5 cm offset fracture oriented parallel to the fault trace. A 2-5 cm displacement oriented 325° NW occurring on a residential structure on top of the fault was observed on the border between Dimasalang and Palanas. The rupture displacement increased further down south ~7 km from the northern shoreline, where a 7 cm left lateral offset was seen coupled with spreading of the road pavement. The fault bisected a coconut tree at the southern limit of the stepover in Palanas (Fig. 10d) (Aurelio, 2022), resulting in a cumulative 87 cm opening from the 2003 and 2020 events. The newer slip is estimated at 27 cm on a 275° W oriented rupture. Right-stepping en echelon fractures occurred adjacent to the coconut tree, most of which were eroded at the time of visit.

The rupture continued southwards to Cataingan, 4 km from the GlobalCMT centroid projection. Fault rupture traversed an abandoned house and deflected a wall for roughly ~50 cm. A soil mound (Fig. 10e), located at the base of the wall, shows a 297° W-oriented rupture with a 48 cm left lateral offset. Residents reported a ~200 m long rupture in the area, which was

https://doi.org/10.5194/egusphere-2023-978
Preprint. Discussion started: 22 June 2023

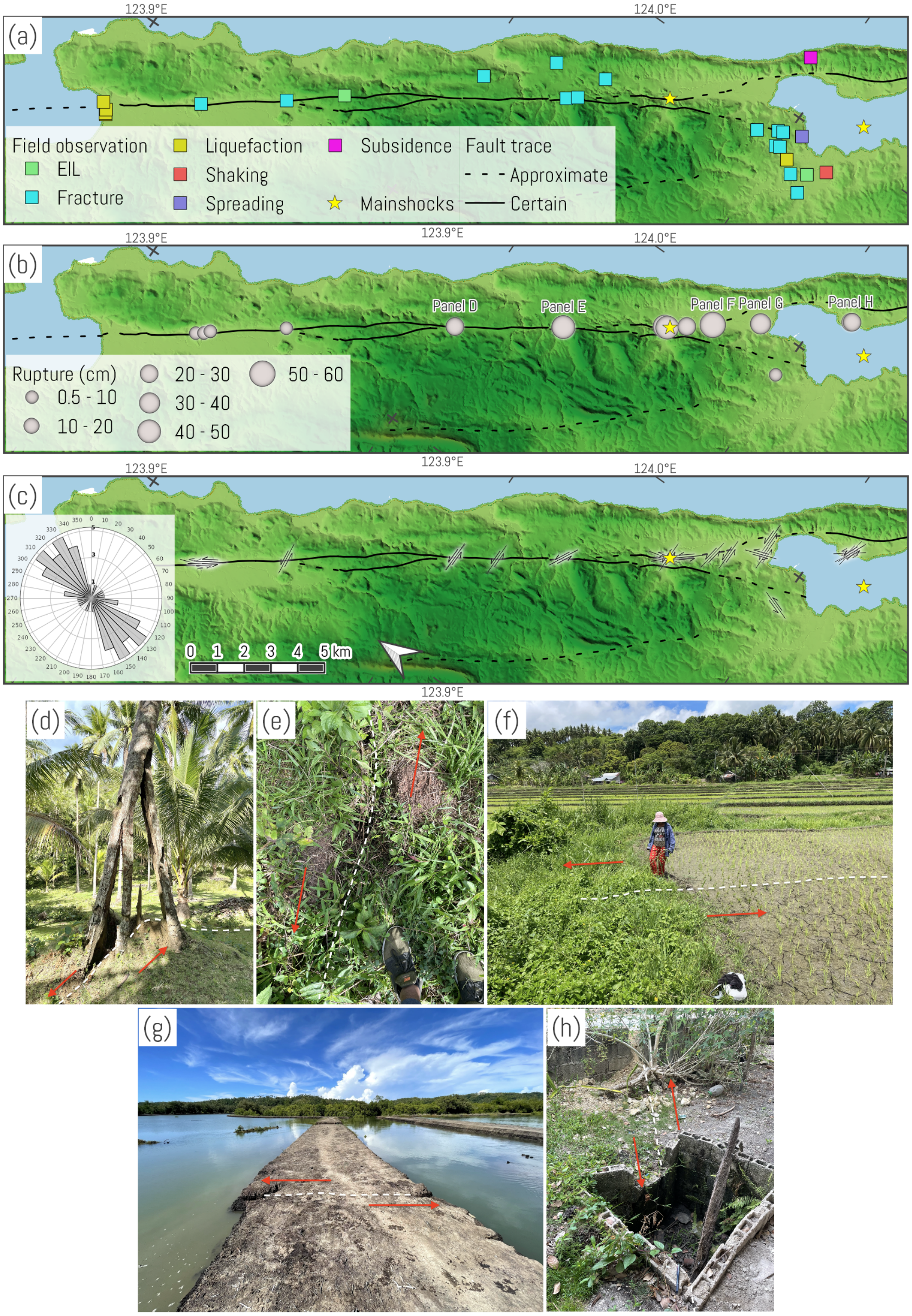

Figure 10. Compiled ground-truthing data. A) Earthquake hazards aside from ruptures. B) Ruptures symbolized by size showing the amount of displacement. C) Rupture orientations. D) Ruptured tree showing cumulative 87 cm slip from 2003 and 2020 events. E) Soil mound cut by the fault highlighting a 48 cm sinistral offset. F) Rice field embankment traversed by fault showing 60 cm displacement. G) Ruptured fishpond dike recording a 34 cm offset. H) Abandoned septic tank showing a 30 cm displacement south of Cataingan Bay.

https://doi.org/10.5194/egusphere-2023-978
Preprint. Discussion started: 22 June 2023

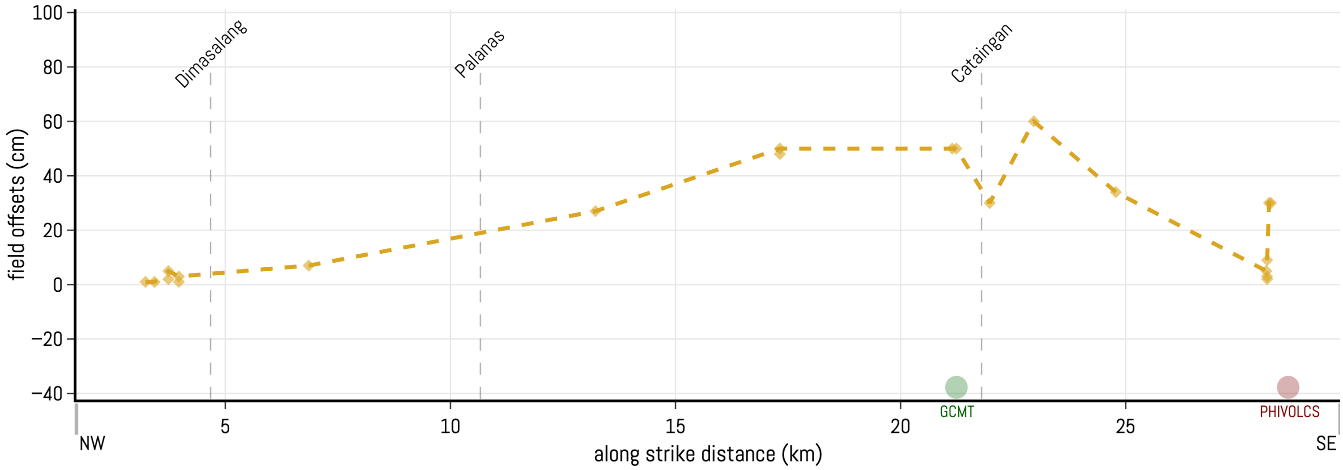

Figure 11. Along strike distribution of measured field offsets.

already mostly eroded. Nevertheless, remnant right-stepping en echelon fractures formed a linear rupture zone connected to the displaced wall. The surface rupture began to bisect the bifurcating fault trace, expressed as a 30 cm rupture across a road in Cataingan. The 279° E-oriented rupture continued south to an agricultural area (Fig. 10f), where the embankments are displaced by ~60 cm, representing the peak field offset measurements. Long, continuous ruptures were observed in the rice fields immediately after the event but were erased by the time of the field investigation. Another southerly continuation was identified, where the 341° NW-oriented rupture displaced fishpond levees (Fig. 10g) by about 34 cm. Locals stated that the visible rupture appeared lengthy and continuous in the deltaic areas immediately after the earthquake. The rupture was evident again south of Cataingan Bay, manifested on a collinear set of points through several residential structures. A septic tank diagonally cut by a 279° NW-oriented rupture, shows a 30 cm left lateral displacement (Fig. 10h). Offset measurements adjacent to the septic tank vary from 5 to 30 cm.

4.4.2 Left-lateral Offset Distribution

The plot of offset features along the fault strike (Fig. 11) shows the minimum 0.5 cm left lateral displacement ~3 km from Naro Bay in Dimasalang. This point corresponds to the northern terminus of the rupture. The measurements continually increased to 50 cm beginning at 17 km from Naro Bay, around the boundary of Palanas and Cataingan. The offset measurements remained constant for a ~4 km span followed by an abrupt dip to 30 cm, which increases again to the peak 60 cm offset. The local 30 cm minimum was measured on a ruptured road. This single discordant measurement could be due to off-fault displacement, physical reduction due to post-earthquake repairs, or an inaccurate measurement from a cultural feature. The displacement tapered to 30 cm near the shoreline of Cataingan Bay. Spatially coincident offsets ranging from 5 to 30 cm resulted in a peculiar trend at the southeastern limitation of the plot. The weighted moving mean curve of the slip distribution (solid green

https://doi.org/10.5194/egusphere-2023-978
Preprint. Discussion started: 22 June 2023

line) for the 2020 Masbate event suggests a 24.5 cm mean sinistral displacement with a maximum of 60 cm near the GlobalCMT centroid projection.

5 Discussion

5.1 Comparison of Optical Correlation and InSAR

5.1.1 Displacement Threshold

Independently applying optical correlation and interferometry to analyze the coseismic and post-seismic periods of the 2020 Masbate event provided a basis to assess the technical capabilities and shortcomings of the methods in a tropical setting. Peak coseismic displacements of the Masbate earthquake amount to ~60 cm, denoting a high interferometric phase gradient for Sentinel-1. SAR interferograms lose coherence when offsets exceed half the interferometric fringe per pixel (Michel et al., 1999), highlighting the effectiveness of the method for small deformations in mm and cm scales (Tronin, 2006).

The ability of InSAR to detect centimetric displacements was evident when comparing the post-seismic and coseismic interferograms. The rupture trace is conspicuous and the displacement is observable in both the near-field and far-field across the fault. Sinistral afterslip was measured from 4 to 14 cm with low 1σ uncertainties. Millimeter-scale offsets were not detected, owing to the resultant 80 m pixel resolution, which is too large to discern fine rupture information. The underestimated coseismic slip of PHIVOLCS (2020) and Tiongson and Ramirez (2022) can be attributed to this limitation, where information is lost due to high phase gradients and near-field decorrelation (Fig. 7).

Optical correlation is useful to assess the near-field region (Avouac et al., 2006) and larger displacements equivalent to at least one-tenth of the pixel resolution (Elliott et al., 2020b; Leprince et al., 2007). Results show that near-field displacements are resolved (Figs. 5 and 6) despite noticeable high noise levels. OIC, using PlanetScope data with 3.125 m pixel resolution, was able to detect sinistral coseismic displacements between 7 to 60 cm in the near-field, but with high 1σ uncertainties than InSAR due to noise. However, careful interpretation of swath profiles is crucial to identify valid measurements because noise easily overprints tectonic signals. Noise signals are amplified by misaligned acquisition geometry, unequal solar illumination angle, and insufficient geometric corrections (Elliott et al., 2020b; Stumpf et al., 2017). The representative 9 April 2020 - 2 April 2021 (satellite ID 1105) images had decent illumination and acquisition geometry agreement (Table 1) and support the validity of the measurements.

5.1.2 Temporal Baseline

The pair classes of PlanetScope orthoimages used in the study showed that images roughly one year apart resolved the rupture far better than those imaged months apart primarily due to the contrasting vegetative cover. Cyclical changes in land cover (Elliott et al., 2020a) necessitate the use of satellite images taken during the same season of the year because similar features assists the algorithm match features for better correlation. Feature matching in agricultural and developing areas can be difficult

https://doi.org/10.5194/egusphere-2023-978
Preprint. Discussion started: 22 June 2023

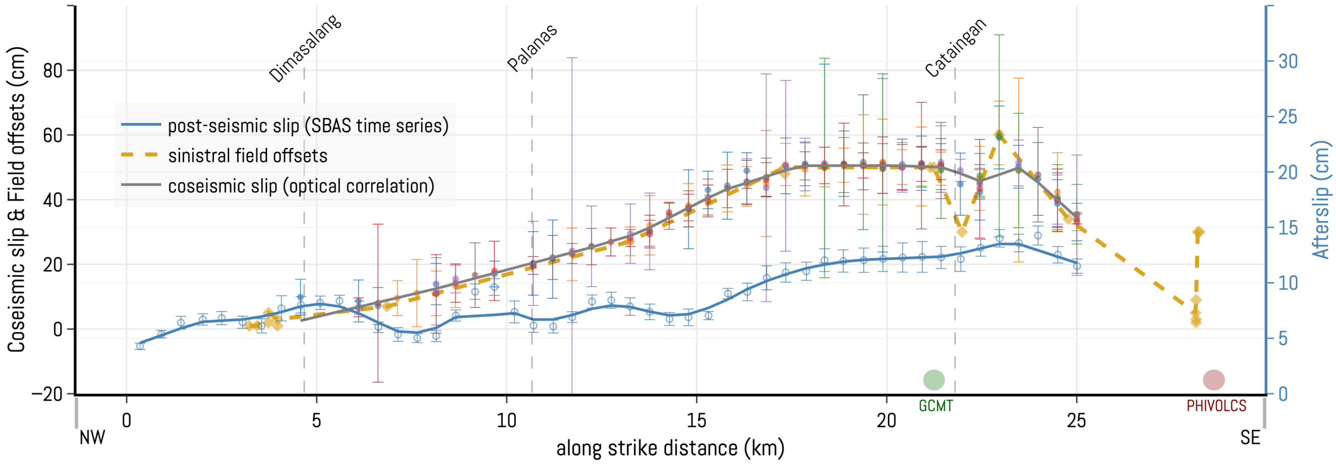

Figure 12. Combined afterslip and coseismic slip distributions. Solid gray line shows the weighted moving mean of the six valid pairs. Dashed yellow line represents the weighted moving mean of the field measurements. Blue line and markers represent the afterslip placed in a secondary axis.

in the subpixel domain given the difference in crop patterns and rapid anthropogenic development, leading to differing pixel intensity values in the pre-event and post-event images (Barnhart et al., 2011).

Images that are one day apart generate deformation fields with minimal seasonal and anthropogenic artifacts. However, this may have exceptions such that correlations for the 2016 Fukushima earthquake using one-day interval drone images resulted in noisy deformation fields with low correlation (Valkaniotis, per. comm., 2021). Single-day intervals were not tested in Masbate due to the lack of usable orthoimagery in terms of study area coverage, relatively similar solar illumination, and cloud cover.

DInSAR relies on coherence to resolve the deformation along the LOS direction, which is controlled by the similarity of point scatterers between the acquisitions. Good coherence in urban areas and dry deserts that remain constant throughout several years produce quality interferograms (Wang and Fialko, 2014; Wei and Sandwell, 2010), which indicate the capability of interferometry to function for longer periods. However, in other types of surface cover such as vegetation and snow, coherence exhibits an indirect relationship with temporal baseline, which reduces the usable time interval (Kervyn, 2001). The six-day revisit of Sentinel-1 conveniently dictates the pre-event and post-event radar data pairing in areas affected by sub-optimal land cover. The baseline can be increased for L-band satellites, such as ALOS-2, for they can detect the bare ground irrespective of surface cover. Interferograms with severe unwrapping errors are manually excluded in the time-series analysis (Yunjun et al., 2019), effectively limiting the temporal baseline range to six to 12 days.

5.2 Accuracy of Optical Correlation

The obtained coseismic slip distribution from optical correlation agrees with the offset feature measurements from the field survey (Fig. 12). The weighted moving mean of the coseismic offsets from optical correlation unifies the measurements from the six valid pairs to compensate for data gaps that particular pairs are unable to resolve. The variance between the two coseismic slip measures for Masbate is typically at ~2 cm with a maximum ~17 cm. The larger difference is interpreted to be

https://doi.org/10.5194/egusphere-2023-978
Preprint. Discussion started: 22 June 2023

a local variation or measurement error since the specific point was taken on a repaired road section, which the remote sensing approach may have missed as it generally detects the overall deformation and is less sensitive to local slip.

Previous studies show varying degrees of misfit between field offsets and remote sensing data (Cheloni et al., 2014; Gold et al., 2021). These were attributed to diffuse displacement, secondary faulting, and shallow fault complexities. Our measured coseismic displacements, however, show consistency and lack of short wavelength variability. This is a consequence of the two-year interval between the earthquake event and the field survey resulting in the eradication of most surface traces and smoothing of the field offset distribution. Furthermore, ruptures on unconsolidated overburden is easily erased due to active weathering and erosion, leaving only the most prominent traces to remain. Similarly, abundant vegetation, challenging surface conditions, and relatively small tectonic displacements compromise the clarity of the resolved rupture and efficacy of optical correlation. Nevertheless, OIC outputs co-validate the field offset measurements and indicate that the remote sensing results are not merely arbitrary results.

The extent of detectable rupture is another fundamental difference between optical correlation outputs and field measurements. The northern rupture terminations are situated 4.6 km and 3.2 km from Naro Bay for optical correlation and field survey, respectively. To the south, OIC measurements cease at the shore of Cataingan Bay since no slip measurements are attainable on the opposite side of the water body, where the field survey revealed more ruptures as the fault resurfaced therein. However, both methods are unable to acquire information in the submerged fault segments.

5.3 Surface Rupture Kinematics

5.3.1 Coseismic Offsets

The amount of coseismic slip is a key factor in the assessment of seismic moment, rupture mechanism, and degree of seismic hazard. The results of this study show a unimodal curve with a characteristic long wavelength and isolated short wavelength variability for the regional slip distribution (Fig. 12). The pattern suggests a low generalized resolution due to temporally-influenced smoothing and noise. The long wavelength offset trend imply overall maturity (Allam et al., 2019), which is a credible interpretation for the Masbate segment of the PF given its Middle Miocene initiation (Fitch, 1972; Tsutsumi and Perez, 2013; Pinet and Stephan, 1990). Furthermore, the known fault trace in Masbate is morphologically linear, supporting the general maturity estimate (Manighetti et al., 2021).

The peak of the unimodal distribution lies ~2 km southeast of the centroid, which implies a relatively simple fault zone (Gold et al., 2021) where the slip is concentrated in the shallow crust. This interpretation, however, requires validation through geodetic inversion. Such peaks usually define the location of the ruptured asperity (Kaneda et al., 2008) where the highest stress drop occurs due to peak moment release from the accumulated potential energy (Freymueller et al., 1994).

By inferring a variable slip signature in the submerged segment coupled with the observed offset variations as the fault resurfaces to the southeast, a mostly vertical rupture propagation with a southwesterly component is suggested (Xu et al., 2010), in accordance with source spectral fitting (Simborio et al., 2022) and indicates a relatively complex shallow submarine fault structure (Llamas and Marfito, 2022).

https://doi.org/10.5194/egusphere-2023-978
Preprint. Discussion started: 22 June 2023

Offset values gradually decay to zero towards the northwest. The smooth slip trend, devoid of short wavelength variation, may suggest a systematic rupture (Treiman, 2002) on a relatively simple sub-vertical fault plane (Allam et al., 2019; Chen et al., 2021). Tapering and deepening aftershock pattern along with the focal mechanism solutions could support this observation. The decreasing slip trend marks the presence of a slip barrier in the north (Xu et al., 2010) due to velocity-strengthening behavior or complex fault geometry (Biasi and Wesnousky, 2017; Bischke et al., 1990) where strain accumulates. This aligns with the known stress accumulation at rupture terminations of most faults (Stein, 2003).

Topography and bedrock geology may also control the rupture (Kaneda et al., 2008), such that the southwestern rupture termination in the study is on an alluvial plain, succeeded by rugged topography northwards. The narrow stepover in Palanas and the bifurcation point in Cataingan coincide with the stratigraphic contacts of the Late Oligocene Nabangig and Miocene-Pliocene Buyag Formations. The fault complexities may reflect the rheological contrast between the clastic limestones of the Nabangig Formation and conglomeratic Buyag Formation.

5.3.2 Post-Seismic Offsets

Post-seismic deformation is usually accommodated as aseismic afterslip, viscoelastic relaxation, or poroelastic rebound (He et al., 2021; Tomita et al., 2020). The coseismic displacement distribution suggests that post-seismic deformation is stress-driven (He et al., 2021) and is mechanically operated as aseismic afterslip (Johanson, 2006) to accommodate the excess co-seismic stress. Our interferometry results revealed a 14 cm peak afterslip, which accounts for 23 % of the peak coseismic displacement over the rapid aftershock decay interval. The six-day revisit cycle of Sentinel-1, however, lead to incomplete measurements since the first radar data in the time-series stack was from 20 August 2020 and was not able to capture the earliest post-seismic deformation immediately after the 18 August 2020 mainshock.

The distribution of afterslip (Fig. 12) along the fault demonstrates a general slip increase southwards, which can be divided into two distinct sections. The northern ~15 km section is characterized by short-wavelength variations and average sinistral offsets of 5-6 cm, whereas the southern section includes the peak afterslip without distinctive variability. The northern trend may indicate the occurrence of diffuse afterslip on a wide zone, which may or may not have breached the surface. Chen et al. (2021) suggested an increased relative friction such that the released post-seismic moment is typically less compared to the mainshock, resulting in heterogeneous loading. However, we cannot exclude the possibility that variability may stem from surface complexities or data processing artifacts, as indicated by observed unwrapping errors and the lack of data from the earliest post-seismic period.

Post-seismic deformation usually occurs outside the regions of peak coseismic slip in normal and thrust faults as stress transfer by the mainshock cause stress loading at the locations of incomplete rupture and unruptured sections (Cheloni et al., 2014; Johanson, 2006; Ozawa et al., 2011; Yagi et al., 2001). However, the results reflect the coincidence of the post-seismic and coseismic slip distributions whose maxima are aligned and equidistant from the centroid accompanied by a gradual slip recession northwards (Fig. 12). This is similar to the 1999 Izmit (Reilinger et al., 2000), 1999 Biak (Das and Henry, 2003), and 2011 Maduo (Wang et al., 2019) earthquakes, which also exhibit spatially overlapping coseismic and post-seismic slip distributions.

https://doi.org/10.5194/egusphere-2023-978
Preprint. Discussion started: 22 June 2023

The findings primarily suggest a vertical stress migration along the fault surface to either deeper or shallower sections of the fault. However, we recognize that the data is limited to surface measurements and more information is required to accurately describe the occurrence of the afterslip along the fault plane. Determining the cause of the superposed slip character of the 2020 Masbate earthquake event is of interest, and warrants investigation into potential factors such as non-steady state friction (Helmstetter and Shaw, 2009), residual stress heterogeneity (Wang et al., 2019), stress reorganization, or shallow material redistribution (He et al., 2021). Additionally, the contribution of known creep associated with the Masbate segment to the slip distributions merits further investigation.

5.3.3 Surface Rupture Length

Surface rupture length estimates from remote sensing data were assumed to be symmetric about the peak displacement zone (Table 5). The coseismic displacement distributions from optical correlation and field survey (Fig. 12) implies that the northern rupture terminus is located approximately 3.2 km from the northern shoreline with the peak slip values occurring between 17.3 to 23.5 km, resulting to rupture length estimates ranging from 28.2 to 41 km. The absence of offset measurements in the submerged portions of the fault necessitated the use of interpolation. Given the asymmetrical nature of strike-slip profiles, which can take on either elliptical or triangular forms (Perrin et al., 2016), caution is critical when interpreting the interpolated values. The rupture lengths are also measured from the total length of the field survey and its extension towards the stepover in Cataingan Bay (Llamas and Marfito, 2022) resulting in 25 and 35.59 km rupture lengths.

5.3.4 Seismic Moment Estimate

Moment magnitude (M_w) and seismic moment (M_o) estimates for the 2020 Masbate event were calculated from the surface rupture parameters (Table 5). M_w calculations were conducted using the corresponding empirical equations from regression of rupture parameters and moment magnitudes (Wells and Coppersmith, 1994). The M_o was derived as a function of M_w from scaling relationships (Hanks and Kanamori, 1979). This approach was preferred over directly calculating the M_o from the rupture area and material rigidity due to the lack of reliable estimates of rupture width and subsurface fault rupture parameters.

The M_w estimates from the maximum and average displacements range between M_w6.50 to M_w6.66, and are similar to the instrumental 6.6 moment magnitude. All rupture length estimates returned high M_w values between M_w6.73 to M_w6.97 which agrees with the 2003 earthquake observations, wherein the fault rupture is longer than expected relative to the magnitude. Comparing the individually calculated M_w values show that the moment magnitude estimates from maximum displacement provide the closest fit with instrumentally determined moment. The accepted M_w6.64 from the maximum displacement is equivalent to a seismic moment of 1.15×10^{19} N·m.

The moment released during post-seismic deformation was assessed using the maximum and average afterslip values (Table 5). The maximum afterslip, which measured 0.14 m, corresponded to a moment magnitude of 6.15, while the average afterslip of 0.09 m yielded a moment magnitude of 6.1. Given that the source parameter of the accepted coseismic moment magnitude is the maximum displacement, the M_w estimate from the maximum afterslip is preferred among the two afterslip parameters.

https://doi.org/10.5194/egusphere-2023-978
Preprint. Discussion started: 22 June 2023

Table 5. Measured rupture parameters with corresponding moment magnitude (Wells and Coppersmith, 1994) and seismic moment (Hanks and Kanamori, 1979).

Parameter	**Value**	M_w	**Mo (N·m)**
Surface rupture length	34.40 km [1]	6.88	2.64×10^{19}
	28.20 km [2]	6.78	1.89×10^{19}
	41.00 km [3]	6.97	3.54×10^{19}
	39.50 km [4]	6.95	3.33×10^{19}
	25.00 km [5]	6.73	1.54×10^{19}
	35.59 km [6]	6.90	2.79×10^{19}
Maximum displacement	0.61 m [7]	6.64	1.15×10^{19}
	0.60 m [8]	6.64	1.14×10^{19}
Average displacement	0.38 m [9]	6.66	1.24×10^{19}
	0.25 m [10]	6.50	6.99×10^{18}
Maximum afterslip	0.14 m	6.15	2.12×10^{18}
Average afterslip	0.09 m	6.10	1.78×10^{18}

[1] symmetrical about the midpoint of the zone of peak displacement
[2] symmetrical about the lower limit of the zone of peak displacement
[3] symmetrical about the upper limit of the zone of peak displacement
[4] symmetrical about the peak displacement
[5] cumulative rupture length from the field survey
[6] cumulative rupture length from the field survey extended to the onshore stepover identified by Llamas and Marfito (2022)
[7] from optical correlation
[8] from field survey
[9] from the weighted moving mean curve of optical correlation outputs
[10] from the weighted moving mean curve of field measurements

The maximum afterslip is equivalent to a M_o of 2.12×10^{18} N·m, indicating that the afterslip resulted in the release of energy equal to 18 % of the mainshock.

5.4 Seismotectonic Implications

5.4.1 Surface Rupture Morphology

The fault geomorphology (Fig. 10c) and geodetic observations (Figs. 5 and 8) highlight the linearity of the Masbate segment. However, the narrow stepover (Tsutsumi and Perez, 2013) around 12°07'N was not clearly defined due to unwrapping errors in interferometry and high-amplitude noise in optical correlations.

The ruptures in Palanas form a right-stepping Riedel shear zone, with the ruptures occurring at a low angle with respect to the regional fault strike. Furthermore, a possible new splay was observed to the south, which potentially represents the primary

https://doi.org/10.5194/egusphere-2023-978
Preprint. Discussion started: 22 June 2023

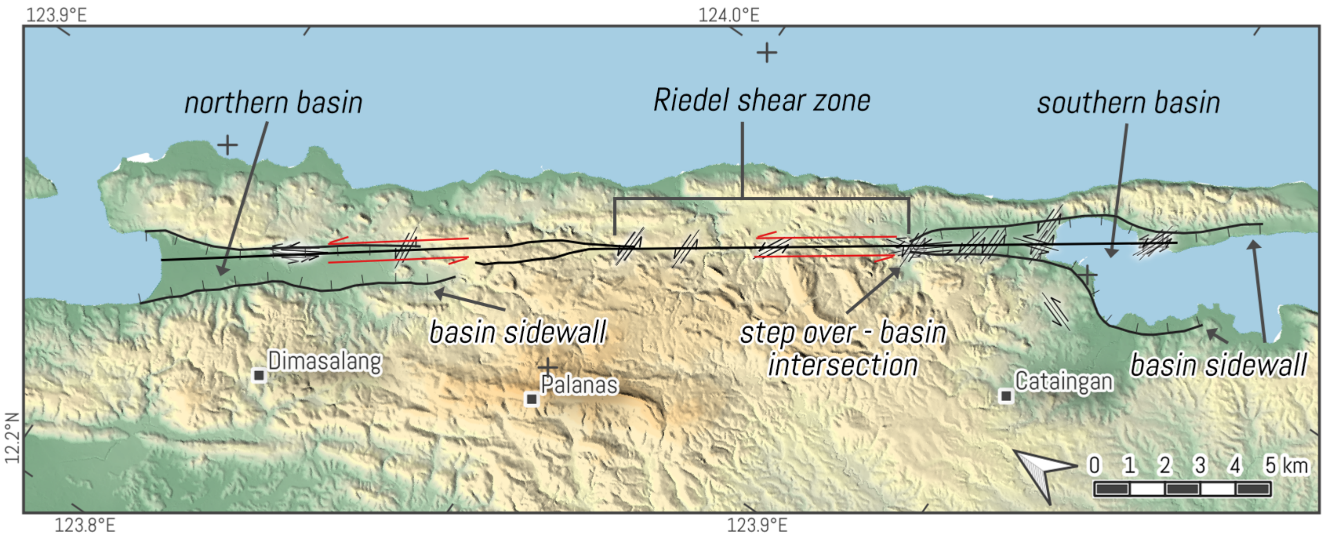

Figure 13. Morphology of the transtensional basins linked by right-stepping shear zone. Solid line indicates the regional fault. Lines with hachures indicate the basin sidewall boundary.

fault plane, cutting across the bifurcating trace and traversing Cataingan Bay. Antithetic shears were observed at the bifurcation point and along the cross-cutting splay.

5.4.2 Developing Transtensional Basins

The morphology of mainland Masbate following the 2020 event (Fig. 13) was the basis of assigning a late relative development stage in a modelled transtensional basin development sequence (Wu et al., 2009). The basin boundary is characterized by floodplains surrounded by topographic highs. Apparent asymmetric depocenters were also recognized, with the shallower depocenter occurring on the floodplain and the nearshore section of Cataingan Bay, while the second one extends further southwest.

A separate transtensional basin is discernible in Dimasalang given the topography, rupture occurrence, and extensional structures in north Masbate (Bischke et al., 1990). The northern and southern basins appear to be linked along the narrow stepover in Palanas. Fault complexities in the principal deformation zone of a pull-apart basin (Wu et al., 2009) impede rupture propagation (Biasi and Wesnousky, 2017) in line with the implications of the observed decreasing coseismic and post-seismic slip towards the north. However, the scarcity of observed ruptures inhibits further analysis of the northern transtensional basin.

Fitting the development stage of the southern basin is constrained by the absence of information regarding local strain partitioning. Nonetheless, the expressed fault maturity and identified negative flower structures (Bischke et al., 1990; Llamas and Marfito, 2022) in the northern and southern bays highlight the presence of oblique extensional stress bounding the Masbate mainland. The orientation of the regional fault implies a WNW-ESE oriented $\sigma 1$. However, real-world conditions are more complex compared to the simplified parameters in the analog model (Wu et al., 2009).

https://doi.org/10.5194/egusphere-2023-978
Preprint. Discussion started: 22 June 2023

6 Conclusions

The necessity of coupling optical correlation and interferometry is demonstrated by investigating the surface rupture of the 2020 M_w6.6 Masbate earthquake along the Masbate segment of the Philippine Fault. Seismicity data showed that foreshocks began 32 days prior to the mainshock on 18 August 2020. The first 30 days of subsequent aftershocks are characterized by a rapid decrease in earthquake frequency, followed by a transition to a gradual decay until 31 January 2021.

Optical correlation and InSAR are directly compared through the corresponding deformation rasters in the coseismic period. Measuring the displacements from the near-field region of the interferogram is hindered by decorrelation, whereas the far-field suffers because of the submerged northeastern block. The optical correlation method revealed an average displacement of 37.7 $\pm$ 10 cm and a maximum displacement of 60.6 $\pm$ 9.8 cm sinistral offsets in the near-field of the onshore fault segments. Both methods are not capable of measuring offshore displacements. The peak sinistral coseismic offset is equivalent to a geodetic moment magnitude of M_w6.64 (1.15×10^{19} N·m).

The capacity of InSAR to detect smaller displacement amplitudes is highlighted by assessing the post-seismic deformation. The SBAS time-series stack outlined a 14.3 $\pm$ 0.9 cm peak afterslip and 8.8 $\pm$ 0.7 cm average sinistral afterslip. The measurements correspond to a M_w6.15 (2.12×10^{18} N·m) energy release equivalent to 18 % of the coseismic moment. The resolved rupture from interferometry is clearer relative to optical correlation. Multimodal rupture length estimates translate to overestimated moment magnitude values. Hence, the Masbate segment is characterized as capable to produce significant slip and ruptures that are longer than expected, despite the short interval and continuous aseismic stress release during interseismic periods.

In terms of accuracy, the optical correlation data agrees with the laterally offset features from field investigation. We interpreted this to be a consequence of the time interval between the 2020 Masbate earthquake and the field investigation. Weathering and erosion of fine ruptures was expected, leading to a smoother field offset distribution.

The coseismic slip distribution shows the presence of a single asperity adjacent to the GlobalCMT centroid. A possible slip barrier exists in the north that may become a strain accumulation zone due to velocity-strengthening properties and shallow fault complexities. Furthermore, the surface distribution of the afterslip coincides with the coseismic slip distribution. Based on the stress transfer theorem, we infer that the afterslip migrated vertically in either the downdip or updip direction along the sub-vertical fault plane.

The surface rupture of the 2020 Masbate event cut across the extant bifurcating trace of the Philippine Fault in the island, possibly reflecting the primary fault plane. Comparing the rupture morphology with analog models reveal the presence of two transtensional basins in Cataingan and Dimasalang, located in the south and north, respectively. The low-angle orientation of ruptures in the midsection correspond to a Riedel shear zone, whereas the stepover is interpreted to link the two identified transtensional basins.

Usage of optical correlation alongside interferometry provides high-resolution surface displacement measurements that can aid in the assessment of earthquake hazards to assist the development of mitigation strategies. We recommend the widespread use of these methods in studying other active faults in the Philippines. In addition, future studies could incorporate other datasets

https://doi.org/10.5194/egusphere-2023-978
Preprint. Discussion started: 22 June 2023

such as UAV data and explore the method for other surface processes. By leveraging the capabilities of these technologies, overall community resilience against earthquake hazards can be improved and ultimately help mitigate the loss of lives and infrastructure damage caused by earthquakes.

Code availability. MicMac is available from github.com/micmacIGN/micmac. StackProf is available from github.com/micmacIGN/stackprof. MintPy is available from github.com/insarlab/MintPy.

Data availability. Sentinel-2 datasets are accessed from ESA/EC Copernicus Sentinels Scientific Data Hub and various repositories. Dataset in this study are retrieved from peps.cnes.fr. Sentinel-1A/B radar data and cloud interferogram processing is available at search.asf.alaska.edu. Planet Labs data are not openly accessible, but academic/scientific access can be requested. Outputs are rendered with Scientific Colour Maps (Crameri, 2021) available from fabiocrameri.ch/colourmaps.

Author contributions. **Khelly Shan C. Sta. Rita:** Conceptualization, Data curation, Formal analysis, Investigation, Methodology, Project administration, Resources, Software, Validation, Visualization, Writing - original draft, Writing - review & editing. **Sotiris N. Valkaniotis:** Formal analysis, Resources, Software, Supervision, Methodology, Writing - review & editing. **Alfredo Mahar Francisco A. Lagmay:** Conceptualization, Funding acquisition, Resources, Supervision, Writing - review & editing.

Competing interests. The authors declare that they have no conflict of interest.

Acknowledgements. We would like to thank the National Mapping and Resource Information Authority for providing the elevation data. We would also like to thank the Philippine Institute of Volcanology and Seismology as well as the Disaster Risk Management office of Dimasalang, Masbate for their contributions to the field investigation.

https://doi.org/10.5194/egusphere-2023-978
Preprint. Discussion started: 22 June 2023

References

Allam, A. A., Kroll, K. A., Milliner, C. W. D., and Richards-Dinger, K. B.: Effects of fault roughness on coseismic slip and earthquake locations, Journal of Geophysical Research: Solid Earth, 124, 11 336–11 349, https://doi.org/10.1029/2018JB016216, 2019.

Allen, C. R.: Circum-Pacific faulting in the Philippines-Taiwan Region, Journal of Geophysical Research (1896-1977), 67, 4795–4812, https://doi.org/https://doi.org/10.1029/JZ067i012p04795, 1962.

Aurelio, M.: Tectonique du segment central de la faille philippine : etude structurale, cinematique et evolution geodynamique, Ph.D. thesis, http://www.theses.fr/1992PA066699, thèse de doctorat dirigée par Rangin, Claude Terre, océan, espace Paris 6 1992, 1992.

Aurelio, M.: Displacement rates and block rotation in and around the Philippines-results from GEODYSSEA data Part II, Program and Abstracts : GEOSEA 98-Ninth Regional Congress on Geology Mineral and Energy Resources of Southeast Asia, 238, https://cir.nii.ac.jp/crid/1570572700614632960, 1998.

Aurelio, M.: Tectonics of the Philippines revisited, Journal of the Geological Society of the Philippines, 55, 119–183, 2000a.

Aurelio, M.: Shear partitioning in the Philippines: Constraints from Philippine Fault and global positioning system data, Island Arc, 9, 584 – 597, https://doi.org/10.1111/j.1440-1738.2000.00304.x, 2000b.

Aurelio, M.: Masbate's three-legged coconut tree spurs scientific interest, https://coverstory.ph/masbates-three-legged-coconut-tree-spurs-scientific-interest/, 2022.

Aurelio, M. and Peña, R.: Geology of the Philippines, 2nd Edition (2010), Mines and Geosciences Bureau, 2010.

Aurelio, M., Barrier, E., Rangin, C., and Müller, C.: The Philippine Fault in the Late Cenozoic tectonic evolution of the Bondoc-Masbate-N. Leyte area, Central Philippines, Journal of Southeast Asian Earth Sciences, 6, 221–238, https://doi.org/10.1016/0743-9547(91)90069-a, 1991.

Aurelio, M., Barrier, E., Gaulon, R., and Rangin, C.: Deformation and stress states along the central segment of the Philippine Fault: implications to wrench fault tectonics, Journal of Asian Earth Sciences, 15, 107–119, https://doi.org/10.1016/s0743-9547(97)00001-9, 1997.

Aurelio, M., Lagmay, M., Escudero, J. A., and Catugas, S.: Latest Philippine earthquake reveals tectonic complexity, Temblor, https://doi.org/10.32858/temblor.191, 2021.

Avouac, J.-P., Ayoub, F., Leprince, S., Konca, O., and Helmberger, D. V.: The 2005, Mw 7.6 Kashmir earthquake: Sub-pixel correlation of ASTER images and seismic waveforms analysis, Earth and Planetary Science Letters, 249, 514–528, https://doi.org/10.1016/j.epsl.2006.06.025, 2006.

Bacolcol, T. C.: Etude géodésique de la faille Philippine dans les Visayas, Ph.D. thesis, Université Pierre et Marie Curie, http://www.theses.fr/2003PA066404, thèse de doctorat dirigée par Barrier, Éric Géologie Paris 6 2003, 2003.

Bacolcol, T. C., Aguilar, A., Jorgio, R., and de la Cruz, R.: Interseismic Deformation and Horizontal Displacements Associated with the February 15, 2003 Masbate Earthquake, Tech. rep., Philippine Institute of Volcanology and Seismology, Philippines, 2005.

Barnhart, W. D., Willis, M. J., Lohman, R. B., and Melkonian, A. K.: Insar and optical constraints on fault slip during the 2010-2011 new zealand earthquake sequence, Seismological Research Letters, 82, 815–823, https://doi.org/10.1785/gssrl.82.6.815, 2011.

Barrier, E., Huchon, P., and Aurelio, M.: Philippine fault: A key for Philippine kinematics, Geology, 19, 32, https://doi.org/10.1130/0091-7613(1991)019<0032:pfakfp>2.3.co;2, 1991.

Bautista, M. L. P. and Oike, K.: Estimation of the magnitudes and epicenters of Philippine historical earthquakes, Tectonophysics, 317, 137–169, https://doi.org/10.1016/s0040-1951(99)00272-3, 2000.

Besana, G. M. and Ando, M.: The central Philippine Fault Zone: Location of great earthquakes, slow events, and creep activity, Earth Planets Space, 57, 987–994, https://doi.org/10.1186/BF03351877, 2005.

Biasi, G. and Wesnousky, S.: Bends and Ends of Surface Ruptures, Bulletin of the Seismological Society of America, 107, 2543–2560, https://doi.org/10.1785/0120160292, 2017.

Bird, P.: An updated digital model of plate boundaries, Geochemistry, Geophysics, Geosystems, 4, https://doi.org/https://doi.org/10.1029/2001GC000252, 2003.

Bischke, R., Suppe, J., and Del Pilar, R.: Implications of a newly discovered branch of the Philippine fault system, in: International Symposium on the Geodynamic Evolution of Eastern Eurasian Margin, 1988.

Bischke, R., Suppe, J., and del Pilar, R.: A new branch of the Philippine fault system as observed from aeromagnetic and seismic data, Tectonophysics, 183, 243–264, https://doi.org/https://doi.org/10.1016/0040-1951(90)90419-9, geodynamic evolution of the Eastern Eurasian Margin, 1990.

Canizares, C., Motagh, M., and Haghshenas Haghighi, M.: Resolving 3D coseismic deformation of the 2019 Mw 7.1 Ridgecrest earthquake using radar and optical data, in: EGU General Assembly Conference Abstracts, p. 13659, 2020.

Chamot-Rooke, N. and Le Pichon, X.: GPS determined eastward Sundaland motion with respect to Eurasia confirmed by earthquakes slip vectors at Sunda and Philippine trenches, Earth and Planetary Science Letters, 173, 439–455, https://doi.org/https://doi.org/10.1016/S0012-821X(99)00239-3, 1999.

Cheloni, D., Giuliani, R., D'Anastasio, E., Atzori, S., Walters, R., Bonci, L., D'Agostino, N., Mattone, M., Calcaterra, S., Gambino, P., Deninno, F., Maseroli, R., and Stefanelli, G.: Coseismic and post-seismic slip of the 2009 L'Aquila (Central italy) MW 6.3 earthquake and implications for seismic potential along the Campotosto fault from joint inversion of high-precision levelling, InSAR and GPS data, Tectonophysics, 622, 168–185, https://doi.org/10.1016/j.tecto.2014.03.009, 2014.

Chen, H., Qu, C., Zhao, D., Ma, C., and Shan, X.: Rupture kinematics and coseismic slip model of the 2021 mw 7. 3 maduo(China) earthquake: implications for the seismic hazard of the kunlun fault, Remote Sensing, 13, 3327, https://doi.org/10.3390/rs13163327, 2021.

Crameri, F.: Scientific colour maps, https://doi.org/10.5281/zenodo.5501399, 2021.

Das, S. and Henry, C.: Spatial relation between main earthquake slip and its aftershock distribution: AFTERSHOCK DISTRIBUTIONS, Reviews of Geophysics, 41, https://doi.org/10.1029/2002RG000119, 2003.

Delorme, A.: StackProf, https://github.com/micmacIGN/stackprof, 2021.

Dianala, J. D. B., Jolivet, R., Thomas, M. Y., Fukushima, Y., Parsons, B., and Walker, R.: The Relationship Between Seismic and Aseismic Slip on the Philippine Fault on Leyte Island: Bayesian Modeling of Fault Slip and Geothermal Subsidence, Journal of Geophysical Research: Solid Earth, 125, e2020JB020 052, https://doi.org/https://doi.org/10.1029/2020JB020052, e2020JB020052 10.1029/2020JB020052, 2020.

Duquesnoy, T., Barrier, E., Kasser, M., Aurelio, M., Gaulon, R., Punongbayan, R. S., and Rangin, C.: Detection of creep along the Philippine Fault: First results of geodetic measurements on Leyte Island, central Philippine, Geophysical Research Letters, 21, 975–978, https://doi.org/https://doi.org/10.1029/94GL00640, 1994.

Elliott, A., Elliott, J., Hollingsworth, J., Kulikova, G., Parsons, B., and Walker, R.: Satellite imaging of the 2015 M7.2 earthquake in the Central Pamir, Tajikistan, elucidates a sequence of shallow strike-slip ruptures of the Sarez-Karakul fault, Geophysical Journal International, 221, 1696–1718, https://doi.org/10.1093/gji/ggaa090, 2020a.

Elliott, J., De Michele, M., and Gupta, H. K.: Earth observation for crustal tectonics and earthquake hazards, Surveys in Geophysics, 41, 1355–1389, https://doi.org/10.1007/s10712-020-09608-2, 2020b.

Farrell, J., Husen, S., and Smith, R. B.: Earthquake swarm and b-value characterization of the Yellowstone volcano-tectonic system, Journal of Volcanology and Geothermal Research, 188, 260–276, https://doi.org/https://doi.org/10.1016/j.jvolgeores.2009.08.008, the Track of the Yellowstone Hotspot, 2009.

Fitch, T. J.: Plate convergence, transcurrent faults, and internal deformation adjacent to Southeast Asia and the western Pacific, Journal of Geophysical Research, 77, 4432–4460, https://doi.org/10.1029/jb077i023p04432, 1972.

Freymueller, J., King, N. E., and Segall, P.: The co-seismic slip distribution of the Landers earthquake, Bulletin of the Seismological Society of America, 84, 646–659, https://doi.org/10.1785/BSSA0840030646, 1994.

GDAL/OGR contributors: GDAL/OGR Geospatial Data Abstraction software Library, https://gdal.org, 2021.

Gold, R. D., DuRoss, C. B., and Barnhart, W. D.: Coseismic surface displacement in the 2019 ridgecrest earthquakes: comparison of field measurements and optical image correlation results, Geochemistry, Geophysics, Geosystems, 22, https://doi.org/10.1029/2020GC009326, 2021.

Hanks, T. C. and Kanamori, H.: A moment magnitude scale, Journal of Geophysical Research: Solid Earth, 84, 2348–2350, https://doi.org/https://doi.org/10.1029/JB084iB05p02348, 1979.

He, L., Feng, G., Wu, X., Lu, H., Xu, W., Wang, Y., Liu, J., Hu, J., and Li, Z.: Coseismic and early postseismic slip models of the 2021 mw 7. 4 maduo earthquake(Western china) estimated by space-based geodetic data, Geophysical Research Letters, 48, https://doi.org/10.1029/2021GL095860, 2021.

Helmstetter, A. and Shaw, B. E.: Afterslip and aftershocks in the rate-and-state friction law, Journal of Geophysical Research: Solid Earth, 114, 2007JB005 077, https://doi.org/10.1029/2007JB005077, 2009.

Johanson, I. A.: Coseismic and postseismic slip of the 2004 parkfield earthquake from space-geodetic data, Bulletin of the Seismological Society of America, 96, S269–S282, https://doi.org/10.1785/0120050818, 2006.

Kaneda, H., Nakata, T., Tsutsumi, H., Kondo, H., Sugito, N., Awata, Y., Akhtar, S. S., Majid, A., Khattak, W., Awan, A. A., Yeats, R. S., Hussain, A., Ashraf, M., Wesnousky, S. G., and Kausar, A. B.: Surface rupture of the 2005 kashmir, pakistan, earthquake and its active tectonic implications, Bulletin of the Seismological Society of America, 98, 521–557, https://doi.org/10.1785/0120070073, 2008.

Kennedy, J. H., Hogenson, K., Johnston, A., Kristenson, H., Lewandowski, A., Logan, T. A., Meyer, F. J., and Rine, J.: Get HyP3! SAR processing for everyone, Tech. Rep. EGU21-8973, Copernicus Meetings, https://doi.org/10.5194/egusphere-egu21-8973, 2021.

Kervyn, F.: Modelling topography with SAR interferometry: illustrations of a favourable and less favourable environment, Computers & Geosciences, 27, 1039–1050, https://doi.org/10.1016/S0098-3004(00)00158-8, 2001.

Krambach, M.: swath profile, https://plugins.qgis.org/plugins/swathProfile/, 2015.

Lagmay, A. M., Tengonciang, A., and Uy, H.: Structural setting of the Bicol Basin and kinematic analysis of fractures on Mayon Volcano, Philippines, Journal of Volcanology and Geothermal Research, 144, 23–36, https://doi.org/https://doi.org/10.1016/j.jvolgeores.2004.11.015, the Tectonics and Physics of Volcanoes, 2005.

Lai, L. C., Rau, R. J., Bacolcol, T., Ker, C. M., Sapla, G., Ching, K. E., and Solidum, Jr., R.: Earthquake Potential of the Creeping-to-locked Masbate Segment of the Philippine Fault Based on GPS Observations, in: AGU Fall Meeting Abstracts, vol. 2019, pp. G43B–0748, 2019.

Legaspi, C. J., Ortega, J. P., Reyes, P. R., and Riza, E. G.: Investigation of Stress Changes along the Philippine Fault Zone Using Coulomb Stress Transfer Modeling, in: GEOCON 2018, 2018.

Leprince, S., Ayoub, F., Klinger, Y., and Avouac, J.-P.: Co-Registration of Optically Sensed Images and Correlation (COSI-Corr): an operational methodology for ground deformation measurements, in: 2007 IEEE International Geoscience and Remote Sensing Symposium, p. 1943–1946, https://doi.org/10.1109/IGARSS.2007.4423207, 2007.

Lindsey, E. O., Fialko, Y., Bock, Y., Sandwell, D. T., and Bilham, R.: Localized and distributed creep along the southern San Andreas Fault, Journal of Geophysical Research: Solid Earth, 119, 7909–7922, https://doi.org/https://doi.org/10.1002/2014JB011275, 2014.

Llamas, D. and Marfito, B.: Geometry and structure of the offshore segments of the Philippine Fault in Central Philippines, in: GeoCon 2022: Disruptions, Transformations—Geosciences at the Forefront, Philippines, 2022.

Manalo, P. C., Dimalanta, C. B., Faustino-Eslava, D. V., Payot, B. D., Ramos, N. T., Queaño, K. L., Perez, A. D. C., and Yumul Jr., G. P.: Geochemical and Geophysical Characteristics of the Balud Ophiolitic Complex (BOC), Masbate Island, Philippines: Implications for its Generation, Evolution and Emplacement, Terrestrial, Atmospheric and Oceanic Sciences, 26, 687, https://doi.org/10.3319/tao.2015.05.19.01(tc), 2015.

Manighetti, I., Mercier, A., and De Barros, L.: Fault Trace Corrugation and Segmentation as a Measure of Fault Structural Maturity, Geophysical Research Letters, 48, e2021GL095 372, https://doi.org/https://doi.org/10.1029/2021GL095372, e2021GL095372 2021GL095372, 2021.

Michel, R., Avouac, J.-P., and Taboury, J.: Measuring ground displacements from SAR amplitude images: Application to the Landers Earthquake, Geophysical Research Letters, 26, 875–878, https://doi.org/10.1029/1999gl900138, 1999.

Mogi, K.: Some Discussions on Aftershocks, Foresocks and Earthquake Swarms : the Fracture of a Semi-infinite Body Caused by an Inner Stress Origin and Its Relation to the Earthquake Phenomena, Bulletin of the Earthquake Research Institute, University of Tokyo, 41, 615–658, https://doi.org/https://doi.org/10.15083/0000033716, 1963.

NDRRMC: Sitrep re Magnitude 6.6 Earthquake in Cataingan, Masbate, https://ndrrmc.gov.ph/index.php/20-incidents-monitored/4096-sitrep-re-magnitude-6-6-earthquake-in-cataingan,-masbate.html, 2020.

Ozawa, S., Nishimura, T., Suito, H., Kobayashi, T., Tobita, M., and Imakiire, T.: Coseismic and postseismic slip of the 2011 magnitude-9 Tohoku-Oki earthquake, Nature, 475, 373–376, https://doi.org/10.1038/nature10227, 2011.

Perrin, C., Manighetti, I., Ampuero, J.-P., Cappa, F., and Gaudemer, Y.: Location of largest earthquake slip and fast rupture controlled by along-strike change in fault structural maturity due to fault growth, Journal of Geophysical Research: Solid Earth, 121, 3666–3685, https://doi.org/10.1002/2015JB012671, 2016.

PHIVOLCS: Historical Earthquakes in the Philippines, 1:5,000,000 map, 1999.

PHIVOLCS: Active Faults Map - Province of Masbate, https://gisweb.phivolcs.dost.gov.ph/gisweb/earthquake-volcano-related-hazard-gis-information, 2018.

PHIVOLCS: 2020 Masbate Earthquake, https://www.phivolcs.dost.gov.ph/index.php/2-uncategorised/10490-2020-masbate-earthquake, 2020.

Pinet, N. and Stephan, J. F.: The Philippine wrench fault system in the Ilocos Foothills, northwestern Luzon, Philippines, Tectonophysics, 183, 207–224, https://doi.org/https://doi.org/10.1016/0040-1951(90)90417-7, geodynamic evolution of the Eastern Eurasian Margin, 1990.

Planet Team: Planet Application Program Interface: In Space for Life on Earth, https://api.planet.com, 2017–.

Porth, H., Müller, C., and von Daniels, C. H.: The sedimentary formations of the Visayan Basin, Philippines, Geol. Jahrbuch Reihe, 1989.

Rangin, C., Le Pichon, X., Mazzotti, S., Pubellier, M., Chamot-Rooke, N., Aurelio, M., Walpersdorf, A., and Quebral, R.: Plate convergence measured by GPS across the Sundaland/Philippine Sea Plate deformed boundary: the Philippines and eastern Indonesia, Geophysical Journal International, 139, 296–316, https://doi.org/10.1046/j.1365-246X.1999.00969.x, 1999.

Reilinger, R. E., Ergintav, S., Burgmann, R., McClusky, S., Lenk, O., Barka, A., Gurkan, O., Hearn, L., Feigl, K. L., Cakmak, R., Aktug, B., Ozener, H., and Toksoz, M. N.: Coseismic and postseismic fault slip for the 17 august 1999, m = 7. 5, izmit, turkey earthquake, Science, 289, 1519–1524, https://doi.org/10.1126/science.289.5484.1519, 2000.

Rosu, A.-M., Pierrot-Deseilligny, M., Delorme, A., Binet, R., and Klinger, Y.: Measurement of ground displacement from optical satellite image correlation using the free open-source software MicMac, ISPRS Journal of Photogrammetry and Remote Sensing, 100, 48–59, https://doi.org/10.1016/j.isprsjprs.2014.03.002, 2015.

Scheffler, D., Hollstein, A., Diedrich, H., Segl, K., and Hostert, P.: AROSICS: An Automated and Robust Open-Source Image Co-Registration Software for Multi-Sensor Satellite Data, Remote Sensing, 9, 676, https://doi.org/10.3390/rs9070676, 2017.

Scholz, C.: Earthquakes and friction laws, Nature, 391, 37–42, https://doi.org/10.1038/34097, 1998.

SEASEE: Series on Seismology Volume IV Philippines, Government Printing Office, 1985.

Seno, T.: The instantaneous rotation vector of the Philippine sea plate relative to the Eurasian plate, Tectonophysics, 42, 209–226, https://doi.org/https://doi.org/10.1016/0040-1951(77)90168-8, 1977.

Simborio, T., Yokoi, T., and Hara, T.: Strong ground motion simulation of the 2020 Masbate, Philippines earthquake (Mw6.6) using Empirical Green's Function method, https://iisee.kenken.go.jp/syndb/data/20230117f70f6a30.pdf, synopsis of IISEE-GRIPS, 2022.

Stein, R.: Earthquake Conversations, Scientific American Sp, 15, 82–89, https://doi.org/10.1038/scientificamerican0705-82sp, 2003.

Stumpf, A., Malet, J.-P., and Delacourt, C.: Correlation of satellite image time-series for the detection and monitoring of slow-moving landslides, Remote Sensing of Environment, 189, 40–55, https://doi.org/10.1016/j.rse.2016.11.007, 2017.

Tiongson, S. and Ramirez, R.: Mapping of ground surface deformations and its associated damage using SAR interferometry: a case study of the 2020 Masbate earthquake, E3S Web Conf., 347, 03 014, https://doi.org/10.1051/e3sconf/202234703014, 2022.

Tomita, F., Iinuma, T., Ohta, Y., Hino, R., Kido, M., and Uchida, N.: Improvement on spatial resolution of a coseismic slip distribution using postseismic geodetic data through a viscoelastic inversion, Earth, Planets and Space, 72, 84, https://doi.org/10.1186/s40623-020-01207-0, 2020.

Treiman, J. A.: Primary surface rupture associated with the mw 7. 1 16 october 1999 hector mine earthquake, san bernardino county, california, Bulletin of the Seismological Society of America, 92, 1171–1191, https://doi.org/10.1785/0120000923, 2002.

Tronin, A.: Remote sensing and earthquakes: A review, Physics and Chemistry of the Earth, Parts A/B/C, 31, 138–142, https://doi.org/10.1016/j.pce.2006.02.024, 2006.

Tsutsumi, H. and Perez, J.: Along strike variation of seismic behavior of the Philippine fault based on historical- and paleo-seismicity, in: AGU Fall Meeting Abstracts, vol. 2011, pp. T43D–2366, 2011.

Tsutsumi, H. and Perez, J.: Large-scale active fault map of the Philippine fault based on aerial photograph interpretation, Active Fault Research, 39, 29–37, https://doi.org/10.11462/afr.2013.39_29, 2013.

Tsutsumi, H., Perez, J., and Lienkaemper, J.: Variation of Surface Creep Rate Along the Philippine Fault Based on Surveys of Alinement Arrays and Offset Cultural Features, in: American Geophysical Union, Fall Meeting 2016, 2016.

Tymofyeyeva, E. and Fialko, Y.: Geodetic Evidence for a Blind Fault Segment at the Southern End of the San Jacinto Fault Zone, Journal of Geophysical Research: Solid Earth, 123, 878–891, https://doi.org/https://doi.org/10.1002/2017JB014477, 2018.

Wang, K. and Fialko, Y.: Space geodetic observations and models of postseismic deformation due to the 2005 M7.6 Kashmir (Pakistan) earthquake, Journal of Geophysical Research: Solid Earth, 119, 7306–7318, 2014.

Wang, S., Xu, W., Xu, C., Yin, Z., Burgmann, R., Liu, L., and Jiang, G.: Changes in groundwater level possibly encourage shallow earthquakes in central australia: the 2016 petermann ranges earthquake, Geophysical Research Letters, 46, 3189–3198, https://doi.org/10.1029/2018GL080510, 2019.

Wei, M. and Sandwell, D. T.: Decorrelation of L-Band and C-Band Interferometry Over Vegetated Areas in California, IEEE Transactions on Geoscience and Remote Sensing, 48, 2942–2952, https://doi.org/10.1109/TGRS.2010.2043442, 2010.

https://doi.org/10.5194/egusphere-2023-978
Preprint. Discussion started: 22 June 2023

Wells, D. and Coppersmith, K.: New Empirical Relationships among Magnitude, Rupture Length, Rupture Width, Rupture Area, and Surface Displacement, Bulletin of the Seismological Society of America, 84, 974–1002, 1994.

Wu, J. E., McClay, K., Whitehouse, P., and Dooley, T.: 4D analogue modelling of transtensional pull-apart basins, Marine and Petroleum Geology, 26, 1608–1623, https://doi.org/https://doi.org/10.1016/j.marpetgeo.2008.06.007, 2009.

Xu, C., Liu, Y., Wen, Y., and Wang, R.: Coseismic slip distribution of the 2008 mw 7. 9 wenchuan earthquake from joint inversion of gps and insar data, Bulletin of the Seismological Society of America, 100, 2736–2749, https://doi.org/10.1785/0120090253, 2010.

Yagi, Y., Kikuchi, M., and Sagiya, T.: Co-seismic slip, post-seismic slip, and aftershocks associated with two large earthquakes in 1996 in Hyuga-nada, Japan, Earth, Planets and Space, 53, 793–803, https://doi.org/10.1186/BF03351677, 2001.

Yunjun, Z., Fattahi, H., and Amelung, F.: Small baseline InSAR time series analysis: Unwrapping error correction and noise reduction, Computers & Geosciences, 133, 104 331, https://doi.org/https://doi.org/10.1016/j.cageo.2019.104331, 2019.